Cell

Article

Single-neuron projectomes of macaque prefrontal cortex reveal refined axon targeting and arborization

Graphical abstract

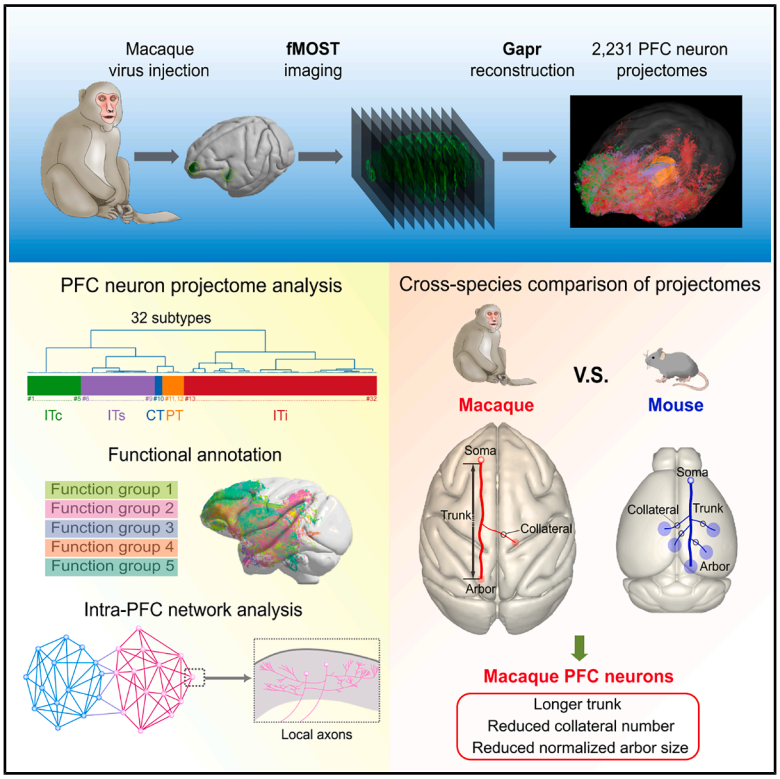

Highlights

- 2,231 single-neuron projectomes were reconstructed for the macaque PFC
- 32 neuron subtypes were classified and their putative functions annotated
- An intra-PFC connectivity network and extensive local axons were uncovered
- Macaque PFC neurons have more refined targeting and axon arbors than mouse neurons

Authors

Lingfeng Gou, Yanzhi Wang, Le Gao, ..., Zhiming Shen, Chun Xu, Jun Yan

Correspondence

yangxiaoquan@brainsmatics.org (X.Y.), zmshen@ion.ac.cn (Z.S.), chun.xu@ion.ac.cn (C.X.), junyan@ion.ac.cn (J.Y.)

In brief

The reconstruction of whole-brain projectomes of 2,231 single neurons from the macaque prefrontal cortex reveals refined axon targeting and arborization, providing a structural foundation for primate-specific cognitive functions.

Gou et al., 2025, Cell *188*, 3806–3822
July 10, 2025
https://doi.org/10.1016/j.cell.2025.06.005

CellPress

CellPress

Cell

Article

Single-neuron projectomes of macaque prefrontal cortex reveal refined axon targeting and arborization

Lingfeng Gou,[1,10] Yanzhi Wang,[1,3,10] Le Gao,[1] Sang Liu,[1] Mingli Wang,[8] Qinwen Chai,[1,3] Jiao Fang,[1,3] Lijie Zhan,[1] Xiaowen Shen,[1] Tao Jiang,[4] Wenqiang Ren,[5] Miao Ren,[5] Xueyan Jia,[4] Chi Xiao,[5] Anan Li,[4,5] Xiangning Li,[4,5] Qingming Luo,[5] Gouki Okazawa,[1,2] Tianming Yang,[1,2] Zhen Liu,[1,7] Mu-ming Poo,[1,2,7] Xiaoquan Yang,[4,5,*] Zhiming Shen,[1,3,7,*] Chun Xu,[1,2,9,*] and Jun Yan[1,6,11,*]

[1]Institute of Neuroscience, CAS Center for Excellence in Brain Science and Intelligence Technology, Chinese Academy of Sciences, Shanghai 200031, China

[2]State Key Laboratory of Brain Cognition and Brain-Inspired Intelligence Technology, Chinese Academy of Sciences, Shanghai 200031, China

[3]University of Chinese Academy of Sciences, Beijing 100049, China

[4]HUST-Suzhou Institute for Brainsmatics, JITRI, Suzhou 215123, China

[5]State Key Laboratory of Digital Medical Engineering, Key Laboratory of Biomedical Engineering of Hainan Province, School of Biomedical Engineering, Hainan University, Haikou 570228, China

[6]School of Future Technology, University of Chinese Academy of Sciences, Beijing 101408, China

[7]Shanghai Center for Brain Science and Brain-Inspired Technology, Shanghai 201210, China

[8]Lingang Laboratory, Shanghai 200031, China

[9]China-Hungary Belt and Road Joint Laboratory on Brain Science, Shanghai 200031, China

[10]These authors contributed equally

[11]Lead contact

*Correspondence: yangxiaoquan@brainsmatics.org (X.Y.), zmshen@ion.ac.cn (Z.S.), chun.xu@ion.ac.cn (C.X.), junyan@ion.ac.cn (J.Y.)

https://doi.org/10.1016/j.cell.2025.06.005

SUMMARY

Cortical expansion endows advanced cognitive functions in primates, and whole-brain single-neuron projection analysis helps to elucidate underlying neural circuit mechanisms. Here, we reconstructed 2,231 single-neuron projectomes for the macaque prefrontal cortex (PFC) and identified 32 projectome-based subtypes of intra-telencephalic, pyramidal-tract, and cortico-thalamic neurons. Each subtype exhibited distinct topography in their soma distribution within the PFC, a characteristic pattern of axon targeting, and subregion-specific patchy terminal arborization in the targeted area, with putative functions annotated. Furthermore, we identified a subdomain connectivity network and extensive local axons within the PFC. Compared with those in mice, macaque PFC projectomes exhibited a similar topographic gradient of terminal arborization at the targeted regions but much higher target specificity, fewer collaterals, and smaller brain size-normalized arbors. Thus, whole-brain single-axon macaque projectomes revealed highly refined axon targeting and arborization, providing key insights into the structural basis for complex brain functions in primates.

INTRODUCTION

The primate prefrontal cortex (PFC), situated at the highest level of cortical hierarchy,[1] integrates sensory inputs with long-term and working memories and executes cognitive control over abstract reasoning, decision-making, task switching, and goal-directed behaviors.[2–6] In the past, inter-areal connectivity of the macaque cortex has been mapped by anterograde and retrograde dye tracing.[7] Recent studies have reported whole-brain projectomes of the macaque and marmoset PFC at the population level using bulk tracing.[8,9] Coarse-grained cortical connectivity of the lateral PFC in macaque has also been revealed by the combined use of electrical microstimulation and functional magnetic resonance imaging (fMRI).[10] However, these previous studies lack the resolution that could resolve branching and arborization patterns of individual axons.

For the mouse PFC, single-neuron projectomes of over 6,300 neurons have been reconstructed, and their whole-brain organizations have been revealed.[11–13] How single-neuron projectomes are organized in the macaque brain, which is two orders of magnitude larger by volume, and to what extent their axon organization exhibits conserved and divergent features from those in the mouse brain are important issues to address. Given the close evolutionary proximity, principles of projectome organization found in macaques will likely be applicable to humans. Although recent technical advances in imaging technologies

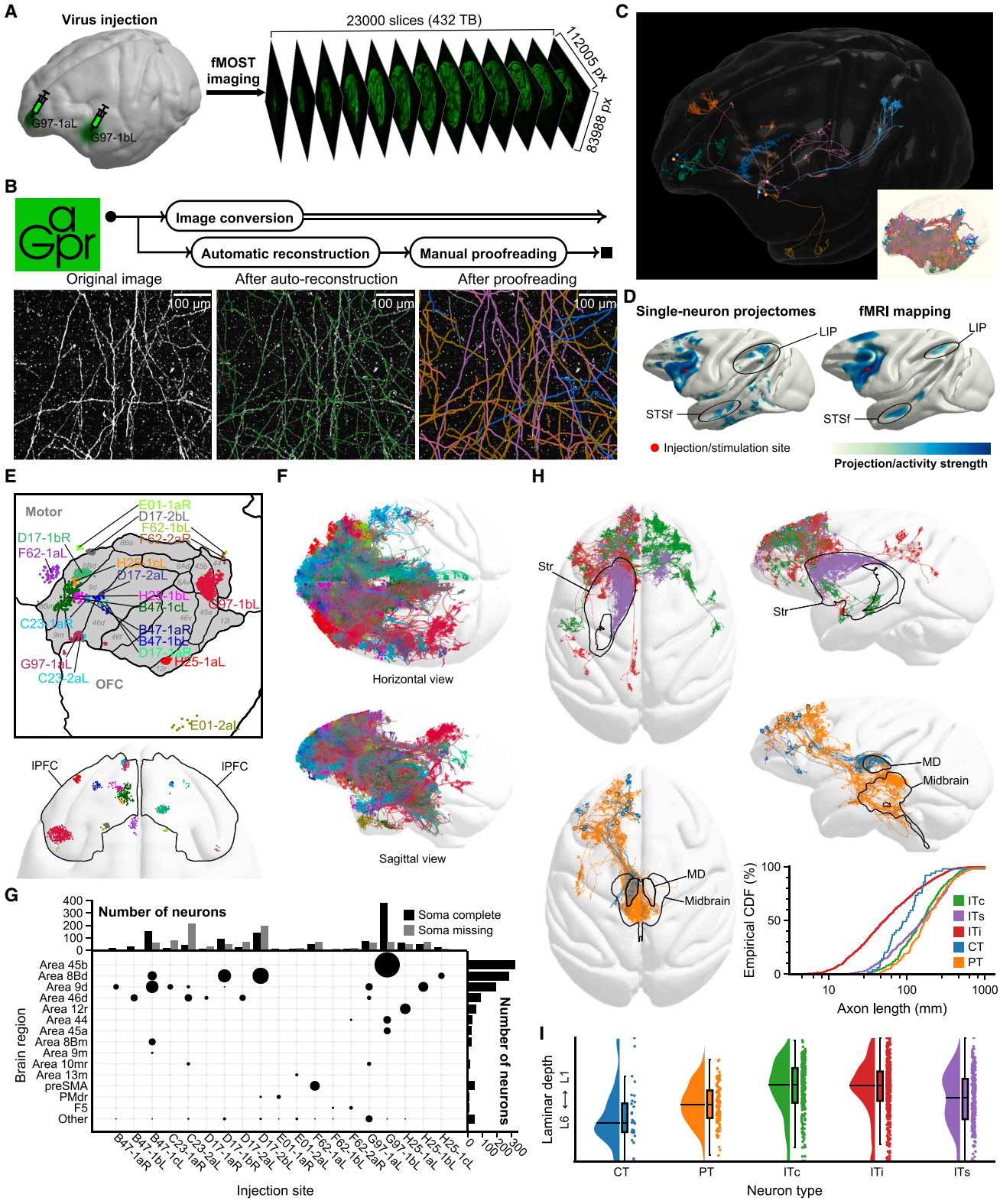

Figure 1. Reconstruction of single-neuron projectomes of macaque PFC

(A) Whole-brain imaging pipeline with fMOST. Virus injection was aided by MRI. 23,000 slices of imaging data at 0.65 μm × 0.65 μm resolution were collected from sample G97.

(legend continued on next page)

such as fluorescence micro-optical sectioning tomography (fMOST)[14] and tissue clearing-assisted light-sheet imaging[15] have made it possible to trace single-neuron projectomes over the entire macaque brain, it remains highly challenging to process large amounts of imaging data and to efficiently and accurately reconstruct single axons for a large number of neurons.

Here, we report a high-throughput mapping of PFC single-neuron projectomes from petabytes (PBs) of imaging data of the macaque brain at micrometer resolution, facilitated by large-scale automatic reconstruction and collaborative proofreading by human annotators. We classified PFC neuron subtypes based on their whole-brain axon projection patterns. Our analyses revealed the subtype-dependent soma distribution within PFC, distinct patterns of axon collaterals, subregion-specific terminal arborizations of macaque PFC neurons, and putative functions of each projectome subtype. Furthermore, we constructed an intra-PFC subdomain network and observed extensive local axons. Comparing macaque PFC projectomes with those in mice, we identified shared correspondence of soma-target topography between the two species. However, we found a general reduction in the number of axon collaterals and in brain size-normalized axon terminal arbors from mice to macaques, resulting in a more restricted target number of a single neuron and smaller relative arbor size at the target zone. Taken together, this study of single-neuron axon organization provides an important basis for understanding neural circuit mechanisms underlying primate brain functions.

RESULTS

Reconstruction of single-neuron projectomes of macaque PFC

We sparsely labeled the neurons in macaque PFC at multiple PFC sites of adult female macaque monkeys (*Macaca fascicularis*) guided by magnetic resonance imaging (MRI) (Figure 1A, left; see STAR Methods and Table S1). The whole-brain axon projections from a total of 19 PFC sites in 7 macaque brains were imaged with fMOST[14] in two color channels at the spatial resolution of $0.65 \times 0.65 \times 3\ \mu m^3$, resulting in a total data size of 432 TB for a single channel of a typical macaque brain (Figure 1A, right). To reconstruct whole-brain axon projections, we utilized a recently developed single-neuron tracing system named Gapr[16] that was optimized for accelerated projectome reconstruction in large datasets of the macaque brain (Figure 1B). Examples of six reconstructed macaque projectomes were shown in Figure 1C. In the example dataset (G97-1), 576 single-neuron projectomes with a total axon length of 94,985 mm were reconstructed by over 50 annotators simultaneously within 12 weeks using approximately 7,200 human hours (Figure S1A; Video S1).

The targeted cortical regions of our projectomes of lateral PFC (lPFC) neurons matched well with the cortical regions that were functionally activated by electrical stimulation of lPFC in fMRI[10] (Figures 1D and S1B–S1D). Furthermore, we found a quantitative agreement between the bulk tracing data using serial two-photon microscopy[9] and our pooled single-neuron projectomes from area 45 in the ventrolateral prefrontal cortex (vlPFC) (Figure S1B, bottom panel, and Figure S1C, top and bottom panel). Finally, our pooled single-neuron projectomes from different areas in the dorsolateral prefrontal cortex (dlPFC) and vlPFC were consistent with the connectivity obtained from retrograde bulk tracing[7] (Figure S1D). Thus, our sampling of single neurons has reached sufficient coverage to represent the overall axon projections.

In total, we reconstructed 2,231 single-neuron projectomes of macaque PFC[17] registered onto a common Monkey Brain Atlas (NIMH Macaque Template version 2.0, NMT v2),[18,19] and somata of these neurons were found in areas 46, 8, and 9 in dlPFC; areas 45 and 12 in vlPFC; and area 10 in the orbitofrontal cortex (OFC) (Figure 1E). The overall projection patterns of the neurons at each injection site were visualized in Figure 1F and Data S1A, and the distribution of virus injection sites was depicted in Figure 1G.

The 2,231 PFC neurons can be divided into three neuron classes: intra-telencephalic (IT) neurons, pyramidal tract (PT) neurons, and cortico-thalamic (CT) neurons[11,20,21] (IT, 2,045; PT, 138; CT, 48). The IT neurons can be further divided into ITi (ipsilateral cortex-projecting only, 1,232), ITs (striatum-projecting, 471), and ITc (contralateral cortex-projecting, 342) (Figure 1H). As illustrated by a specific injection site at area 45 (Figure S2A), the somata of subcortically projecting PT and CT neurons were distributed in infragranular layers (L5/6), while neurons projecting intra-cortically, including ITi and ITc neurons, were mainly distributed in supragranular layers (L2/3), and striatum-projecting ITs neurons were found in both infragranular and supragranular layers (Figure 1I).

Projectome-based classification of macaque PFC neuron subtypes

We next classified all PFC neurons into 32 projectome-based "subtypes" by the overall morphological similarity of single-neuron projectomes[11] (Figure 2A). The preferential targets for each subtype were highlighted in Figure 2A. Overall, subtypes 1–5 (ITc neurons) displayed contralateral cortical projection.

(B) Reconstruction workflow of single-neuron projectomes with Gapr[16] (dataset G97-1 as an example on the bottom right). Scale bars, 100 μm.
(C) Projectomes of six representative neurons (randomly color-coded) from dataset G97-1. Shown in the bottom right is the whole-brain projectome of all reconstructed neurons in dataset G97-1.
(D) Comparison of our projectomes with fMRI data upon stimulation at a corresponding site in vlPFC.[10]
(E) Soma distribution of all reconstructed neurons, color-coded by injection sites.
(F) Overview of whole-brain projectomes, color-coded by injection sites (a maximum of 100 neurons shown per site).
(G) Regional distribution of neurons across injection sites, with dot size (area) denoting neuron number.
(H) Examples of IT, PT, and CT neurons and the empirical cumulative distribution function (ECDF) of total axon length for all neuron types.
(I) Laminar distributions of somata for five neuron types across all samples. The black lines in the density plots indicate median values. The boxplot of cortical soma depth for each neuron type is bounded between 0 and 1, with the interquartile range (IQR) represented by the box, the whiskers lying within both the data range and 1.5×IQR, and individual soma positions shown with dots on the right.
Related to Figures S1 and S2.

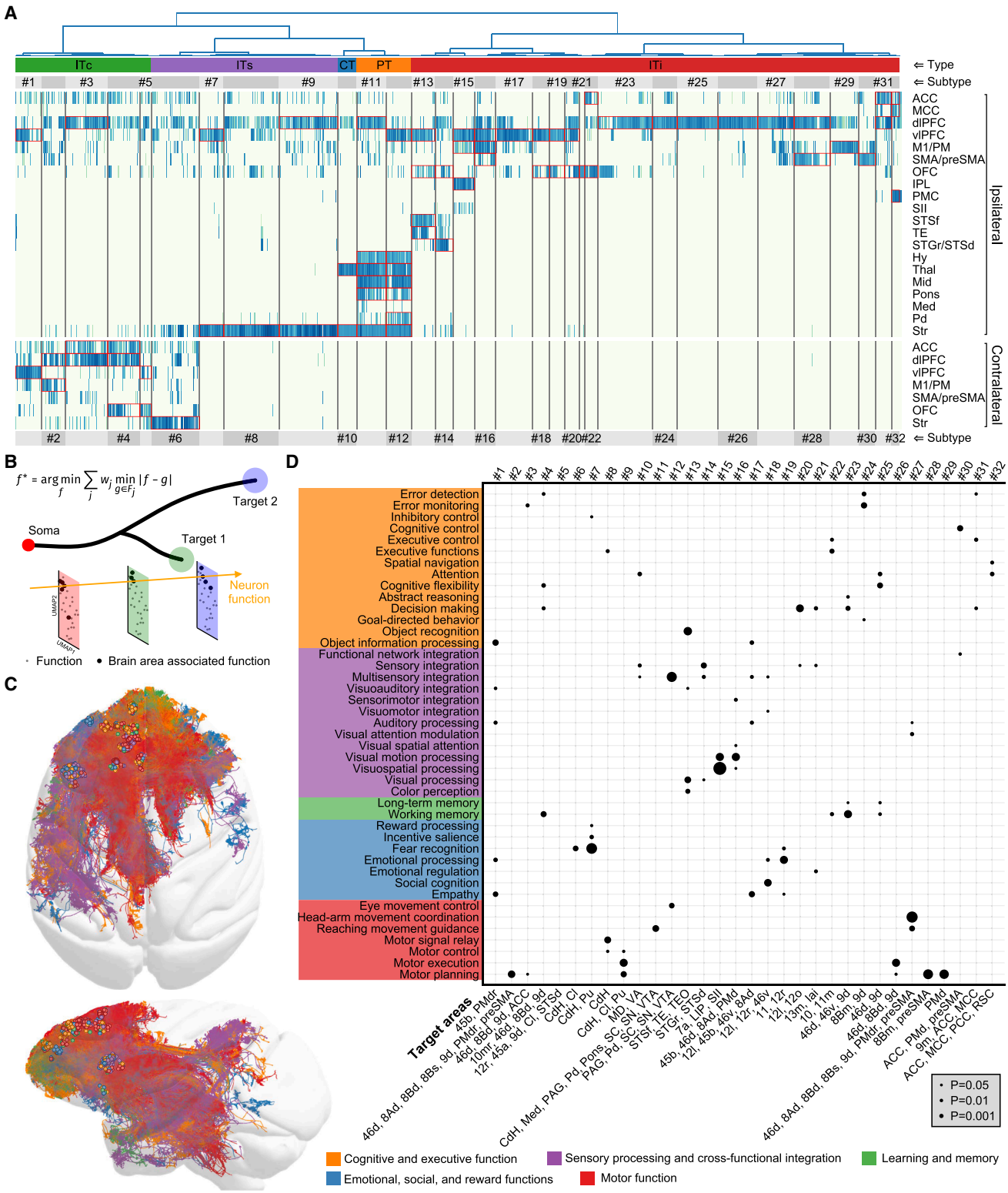

Figure 2. Projectome-based classification of macaque PFC single-neuron projectomes

(A) Clustering of all neurons into 32 subtypes by axon morphology, with a heatmap of projection strength across brain regions as the logarithm of axon length to major targeted brain regions.

(legend continued on next page)

Subtypes 6–9 (ITs neurons) projected to the striatum. Subtypes 13, 14, 15, and 32 exhibited long-range ipsilateral projection to parietal and temporal lobes. Subtypes 11 and 12 corresponded to PT neurons, and subtype 10 corresponded to CT neurons. The relationship of these subtypes based on their morphology is shown on the uniform manifold approximation and projection (UMAP) after dimension reduction (Figure S2B), and the morphology of all subtypes is shown in Data S1B.

We next quantified the projection diversity of neurons at the same virus injection sites and found that almost every single injection site harbored multiple subtypes (Figure S2C), suggesting diverse projections even among closely situated neurons in PFC. Furthermore, the somata of most subtypes were found at multiple injection sites, but the soma distribution of each subtype showed preference for specific PFC areas (Figure S2D, top) and distinct cortical layers (Figure S2D, bottom). Together, our single-neuron projectome subtype analysis reveals that the somata of neurons in each subtype could be found in many PFC regions, but there were clear area- and layer-preferences in their distribution, similar to those found for mouse PFC projectome subtypes.[11]

To examine the potential functions of these projection-based subtypes, we first manually compiled functional annotations for all macaque brain areas (see STAR Methods; Table S2). We developed an algorithm (see STAR Methods) to provide the functional annotation of the neuron with the known function that is most congruent between the PFC area where the soma was located and its targeted areas (Figure 2B). We then identified the enriched functions associated with neurons within each projectome subtype (Figures 2C and 2D). For example, we found that subtype 13 (projecting from area 45b to inferior temporal cortex [TE]) is enriched with object recognition, subtype 15 (projecting from area 45b to the lateral intraparietal area [LIP]) with visuospatial processing, subtype 19 (projecting from area 12r to area 11) with emotion, and subtype 27 (projecting from area 8Bd to the dorsal premotor cortex [PMd] and pre-supplementary motor area [preSMA]) with reaching movements. Note that the first two examples confirm the known functions of the projections, whereas the latter two examples represent previously unreported functions of PFC projections from these areas. Overall, these putative functional associations encompass cognitive, sensory, emotional, and motor processing functions, highlighting the functional diversity among distinct macaque PFC projectome subtypes.

Long-range cortico-cortical projectomes of PFC ITi neurons

We found that PFC top-down projections were mainly provided by ITi subtypes 13/14 and 15/32 to specific areas within the temporal lobe and parietal lobe, respectively (Figure 3A). The somata of subtypes 14/32 and 13/15 were mostly localized to L3 of dlPFC and vlPFC, respectively (Figures S2D and 3B). These neurons specifically targeted either the temporal or parietal lobe, but rarely both lobes (Figure 3A, bottom right, and Figure 3C), as shown in the example in Figure 3D. Notably, the somata of different subtypes projecting to either parietal or temporal lobe were locally intermingled, varying only slightly ($p = 0.036$) in their laminar depths within L3 (Figures 3E and 3F), suggesting potential local PFC integration for feedback regulation.

The projection targets of these four ITi subtypes exhibited selective topography along mediolateral and dorsoventral axes (Figures 3A and 3C). Temporal lobe-projecting subtypes 14 (somata in dlPFC) and 13 (somata in vlPFC) showed preferential projections to the dorsal bank of the superior temporal sulcus (STSd) and TE in the temporal lobe, respectively (Figure 3G), indicating the respective preference of temporal projections for dlPFC and vlPFC neurons (Figure 3H). This is in line with the previous reports that TE connects with vlPFC[22] and anterior of the superior temporal sulcus (STS) connects with the dorsal area of dlPFC in auditory processing,[23] and consistent with fMRI data upon electrical microstimulation (Figure 3I).[10] Additionally, parietal lobe-projecting subtypes 32 and 15 showed exclusive projections to the posterior cingulate cortex (PCC) and LIP in the medial and lateral parts of the parietal lobe, respectively (Figures 3J and 3K). The somata of subtype 32 were found in the medial dlPFC, which is known to project to the cingulate cortex involved in the default mode network and related to spontaneous thought processes and resting-state mind activity.[24,25] In comparison, the somata of subtype 15 were in a region within the lPFC that is reciprocally connected with LIP[26] and plays key roles in saccade planning, spatial attention, and decision-making.[27] These single-neuron projectomes provide the structural basis for such topographic functional connectivity between the PFC and other cortical areas.

We extracted over 17,000 terminal arbors from the single axons using a machine-learning-based method for identifying the arbors of a single macaque neuron (Figures S3A and S3B; see STAR Methods). Clustering of the cortical arbors based on their laminar distribution revealed six types of arborization patterns (Figure S3C; see STAR Methods). Among them, types 4, 5, 6, 2, and 1 arbors were located progressively from superficial to deep layers (Figure S3D). By contrast, type 3 arbors showed a columnar pattern and a broad laminar distribution (Figure S3E). We then examined the whole-brain distributions of these six arbor types (Figure S3F). We found that the proportion of type 4 arbors, located in the most superficial layer, is highest in TE, whereas that of type 1 arbors, located in the deepest layer, is highest in PCC (Figure S3G), consistent with the different laminar distributions of terminal axons in these targeted areas (Figures 3L and 3M). Thus, PFC neurons serving top-down feedback regulation exhibited diverse patterns of terminal arborization at their targeted areas. We summarized the organization of PFC long-range cortico-cortical projections in Figure 3N.

Subdomain network of intra-PFC axon connections

To examine the fine-grained intra-PFC connectivity, we first defined 44 PFC subdomains containing densely distributed arbors and/or somata (see STAR Methods, Figures 4A and 4B).

(B) Functional annotation of individual neurons by integrating functional categories of somata and targets.
(C) Whole-brain projections of all PFC neurons colored by functional categories.
(D) Functional enrichment for the 32 projection-based subtypes. The relative sizes of the points in the plot reflect the correspondence p values of significance.
Related to Figures S2.

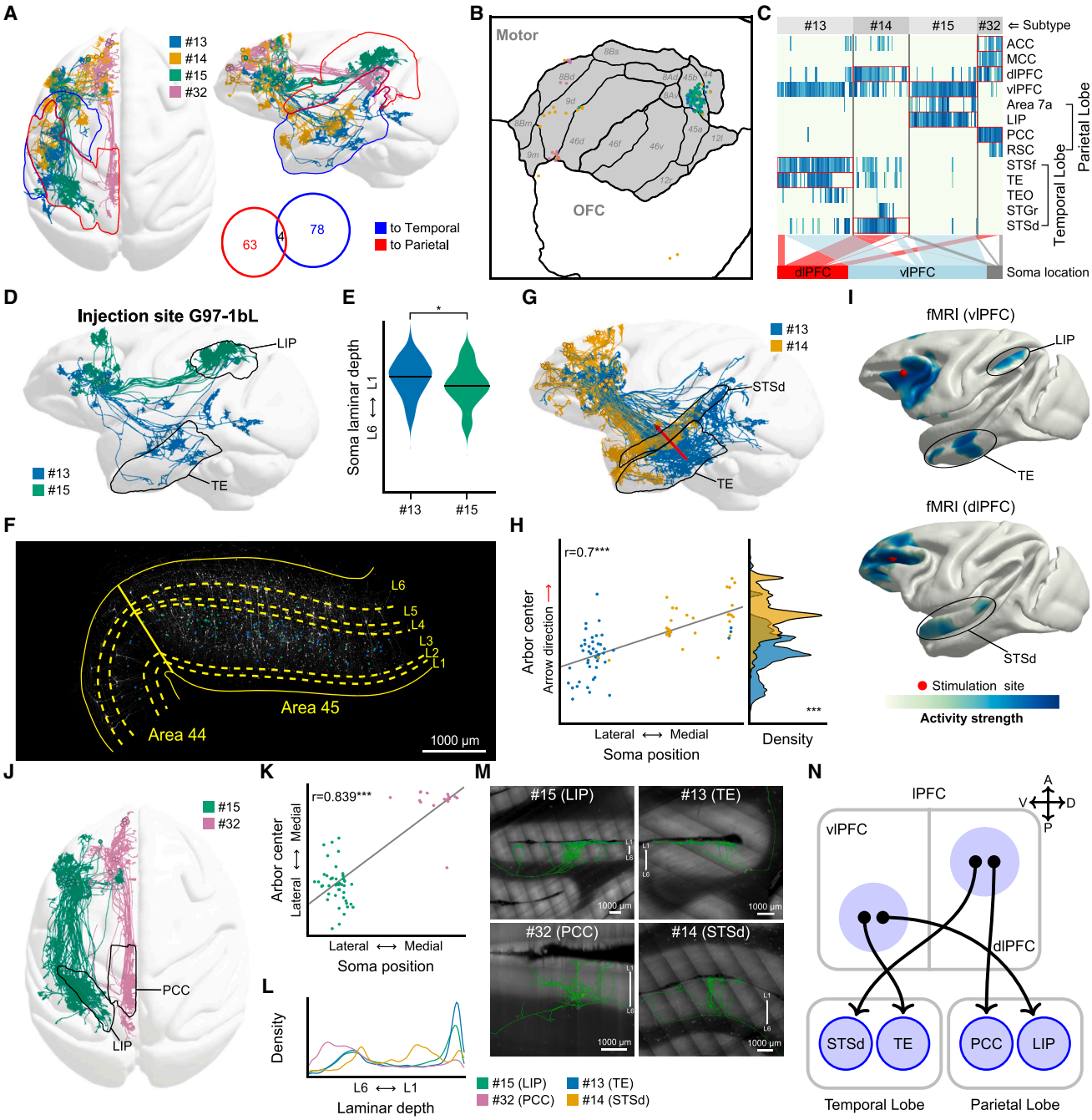

Figure 3. Long-range cortico-cortical projections of macaque PFC ITi neurons

(A–C) Four ITi neuron subtypes (#13–15 and #32) projecting to parietal and temporal cortices (A), with their soma distributions (B), and projection strengths shown as heatmap (C).

(D–F) Subtypes #13 and #15 projecting preferentially to TE and LIP, respectively, with laminar distributions of somata shown. The median laminar soma depth is labeled with a black line in (E) for each subtype. Scale bar in (F), 1,000 μm.

(G and H) Subtypes #13 and #14 showing topography between soma positions and axon terminal arbors.

(I) Responses of fMRI signals upon vlPFC and dlPFC stimulation.[10]

(J and K) Subtypes #15 and #32 showing topography between soma positions in lPFC and axon terminals in parietal cortex.

(L and M) Subtype-specific laminar distributions of axon terminal arbors. Scale bars in (M), 1,000 μm.

(N) Organization rules of dlPFC/vlPFC neurons projecting to parietal and temporal lobes. For the orientation indicator, A, anterior; P, posterior; D, dorsal; V, ventral.

For statistical significance, $^{*}p < 0.05$, $^{***}p < 0.001$.

Related to Figures S3.

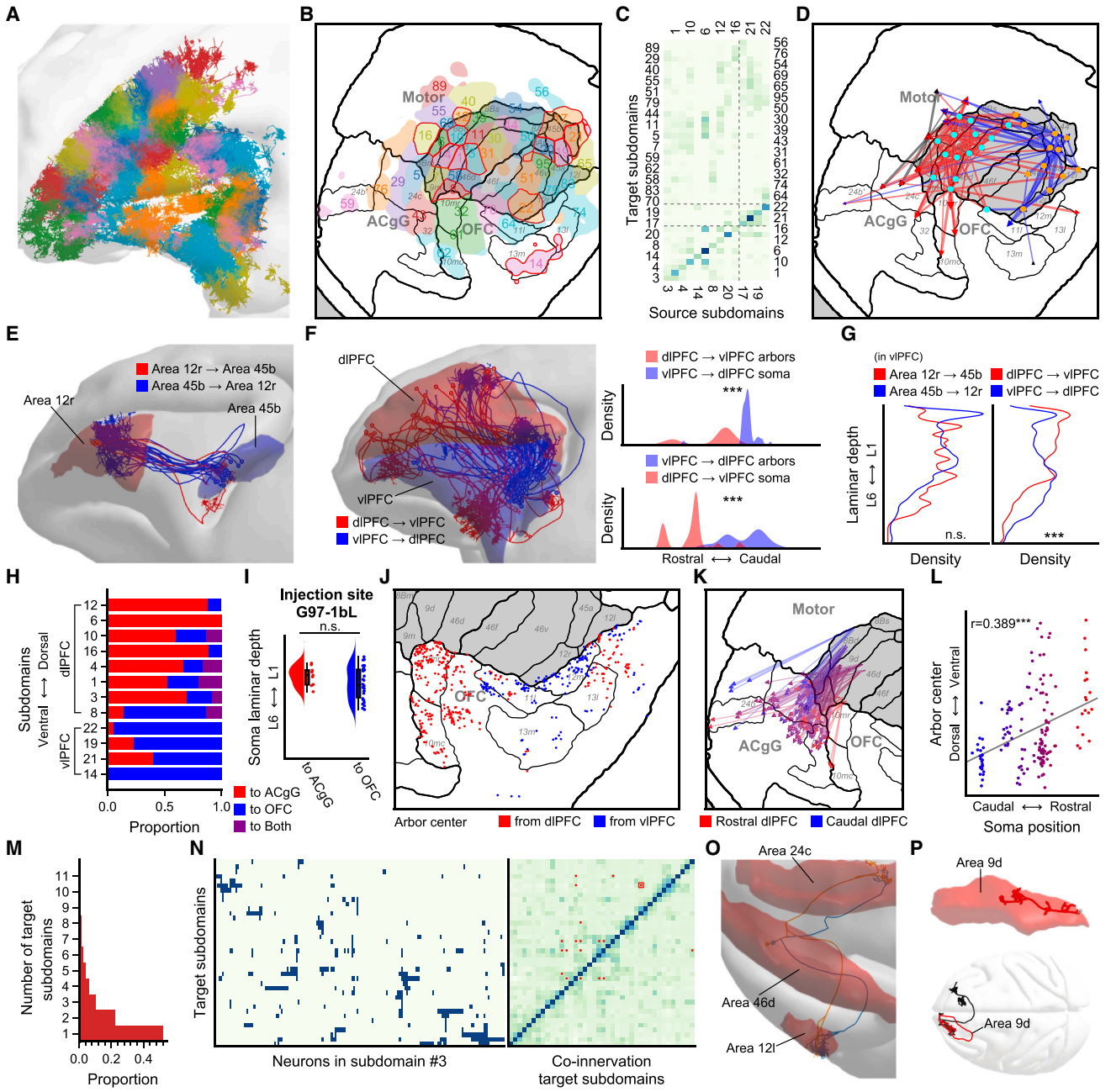

Figure 4. Subdomain network of macaque intra-PFC axon connections

(A and B) Identification of 44 intra-PFC subdomains by clustering of axon arbors and somata; 14 subdomains with ≥10 neurons outlined in red (B).

(C and D) Normalized projection matrix (C) and intra-PFC connectivity network (D) among subdomains, with modular subdomains highlighted in (D) (dlPFC, cyan; vlPFC, orange).

(E–G) Reciprocal vlPFC connections in areas 45b and 12r (E), segregated dlPFC/vlPFC connections (F), and their laminar distributions of axon arbors (G).

(H and I) Proportions of ACgG- and OFC-projecting neurons in dlPFC/vlPFC subdomains (dorsoventrally ordered) (H), with laminar soma distributions from one injection site shown (I) (the median and quartiles are shown by the box of the boxplot for each projection type, with whiskers lying within both the data range and 1.5 × IQR).

(J) Distributions of OFC arbor centers from dlPFC/vlPFC neurons.

(K and L) Rostral/caudal dlPFC projections to ACgG (K) and the correlation between somata and arbor centers (L).

(M) Proportions of the number of targeted ipsilateral PFC subdomains by individual ITi neurons.

(N and O) Projection matrices of subdomain #3 (area 46d, dlPFC) and co-innervation of all target subdomains (N), with an example joint projection to subdomains #76 and #83 shown (O).

(P) An example of local axon in area 9d from a contralaterally projecting neuron.

For statistical significance, n.s., not significant; ***$p < 0.001$.

Related to Figures S4 and S5.

Among them, 14 subdomains (with red contours in Figure 4B) contained at least 10 somata of source neurons besides arbors. Based on the projection strength matrix from the soma-containing subdomains to all target subdomains (Figure 4C), we constructed an intra-PFC connectivity network (Figures 4D and S4A). Through network analysis, we identified two modules in lPFC, each containing the highly interacting subdomains roughly corresponding to dlPFC and vlPFC, respectively (Figure 4D).

We found that the neurons within each lPFC module sent axon projections in a reciprocal manner between subdomains of the same module via a common axon bundle in the white matter, as shown by an example of connectivity between subdomains in areas 45b and 12r, both in the vlPFC module (Figure 4E), and may be involved in object-oriented behavior and eye movement regulation.[28,29] Furthermore, we found that dlPFC and vlPFC modules were also connected by recurrent projections mediated by different receiving and sending subdomains in the two modules, as shown in Figure 4F. Interestingly, the cortical arborization of reciprocal connections within a module and cross-module recurrent connectivity both appeared to show similar laminar distribution (Figures 4G and S4B, top two panels), suggesting that these dlPFC and vlPFC neuron groups may be at a similar cortical hierarchy level. Such cross-module connections may facilitate the integration of sensory information from the ventral pathway with action commands from the dorsal pathway to finalize motor decisions.[30]

In our study, we observed preferential projections from neurons in lPFC subdomains to other PFC subdomains in either the anterior cingulate gyrus (ACgG) or OFC, with fewer neurons projecting to both areas (Figure S4C). The percentages of ACgG-projecting neurons in dlPFC subdomains were higher than those in vlPFC subdomains, and the opposite was found for OFC-projecting neurons (Figures 4H and S4D). The somata of ACgG- and OFC-projecting neurons were intermixed across cortical layers with no significant laminar preference (Figure 4I). Furthermore, while both dlPFC and vlPFC neurons projected to OFC, they projected to different subdomains of OFC, with dlPFC and vlPFC axon arbors located in more dorsal (areas 10mr and 10mc) and ventral (areas 11l and 12m) OFC subdomains, respectively (Figure 4J). Finally, among the dlPFC neurons projecting to ACgG, we identified a fine-grained topographic correspondence between soma and arbor distribution (Figure 4K), in which rostrally located dlPFC neurons preferentially projected to more ventral subdomains of ACgG (Figure 4L). For projections to ACgG, we found that arborizations originating from the dlPFC tended to terminate slightly more superficially than those from the vlPFC (Figure S4E, left, and S4F, left two panels). By contrast, for projections to OFC, arborizations from the dlPFC were predominantly located in the deep layers, whereas those from the vlPFC were distributed across the superficial and middle layers (Figure S4E, right, and S4F, right two panels). Thus, lPFC projections to ACgG and OFC were segregated at the single-neuron level, and neurons in vlPFC and dlPFC modules exhibited different regional topography and different laminar preferences of axon arborization in ACgG and OFC.

To delineate the collateral branching patterns of PFC neurons, we conducted co-innervation analyses (see STAR Methods) for all labeled neurons located in each lPFC subdomain. While most lPFC neurons with intra-PFC projections were found to project to a single PFC subdomain (Figure 4M), we also identified many cases of enriched motifs of joint projections from different neurons (Data S1C). As an example, we obtained the projections of single neurons in lPFC subdomain 3 (area 46d) to other PFC subdomains, as represented by a heatmap (Figure 4N, left). Among the co-innervation matrix, defined as the correlation of projection strengths from subdomain 3 neurons between all subdomain pairs (Figure 4N, right), we found an enriched motif of joint projection of subdomain 3 neurons to two distant subdomains, i.e., subdomain 77 (area 24c in ACgG) and 81 (area 12l in vlPFC) (Figure 4O). Therefore, a single macaque PFC neuron could send axon collaterals to two different PFC subdomains, allowing them to transmit signals to multiple specific PFC areas.

Local recurrent excitatory connections by so-called intrinsic axons allow PFC neurons to sustain activities without external sensory inputs.[31] In our single-neuron reconstruction, we identified numerous intrinsic axons of single neurons extending horizontally (Figure S5A; Figure S5B as an example of intrinsic axons in area 8Bd), similar to those previously reported for neurons within layer 3 of area 9/46 in macaque.[32,33] In addition to the area 9/46, intrinsic axons with the horizontal connectivity pattern can be found at area 8Bd in dlPFC and area 45b in vlPFC (Figure S5C), suggesting that extensive horizontal connectivity is common in PFC. Interestingly, we found that the same neurons containing intrinsic axons also projected to contralateral cortical areas (Figure 4P; Figures S5C, #1, #4, and #5), consistent with previous reports.[34–37] Similar intrinsic axons with the local connectivity were also found in the mouse PFC in our previous study[12] (Figure S5D). In summary, our findings revealed the ubiquitous presence of horizontally extended intrinsic axons within the macaque PFC, with potentially important roles in connectivity organization of local circuit.

Contralateral and striatal projections of PFC IT neurons

Contralateral cortical projections via corpus callosum coordinate the activity and information transfer between the two hemispheres.[38] We analyzed the projection patterns of PFC ITc neurons (Figure 5A) and found few ITc neurons projecting to distant cortical targets in parietal and temporal regions, consistent with the previous report.[39] The ITc projectome subtypes 1–5 were distinguished by the contralateral projections to their respective homotypic cortical areas (Figure 5B). The contralateral arbors of a single ITc neuron generally extended within the range of ~1 cm around the mirrored location of its soma in the homotypic area (Figure 5C), resulting in a strict correspondence of ipsilateral soma locations and contralateral arbor centers (Figure 5D). However, the topography of the soma location was preserved in the main axon location at the midline cross-section of the corpus callosum only along the anteroposterior axis (Figure 5E) but not the dorsoventral axis of PFC (Figure S6A). Such axon arrangement within the corpus callosum may result from signaling molecules acting as guidance cues during development.[40] As quantified by the hemispheric bias index (see STAR Methods), ITc neurons predominantly targeted contralateral homotypic cortical areas (Figure 5F). Furthermore, the extent of contralateral bias of ITc neurons was correlated with the soma location along the dorsoventral axis, resulting in higher bias in vlPFC than in dlPFC.

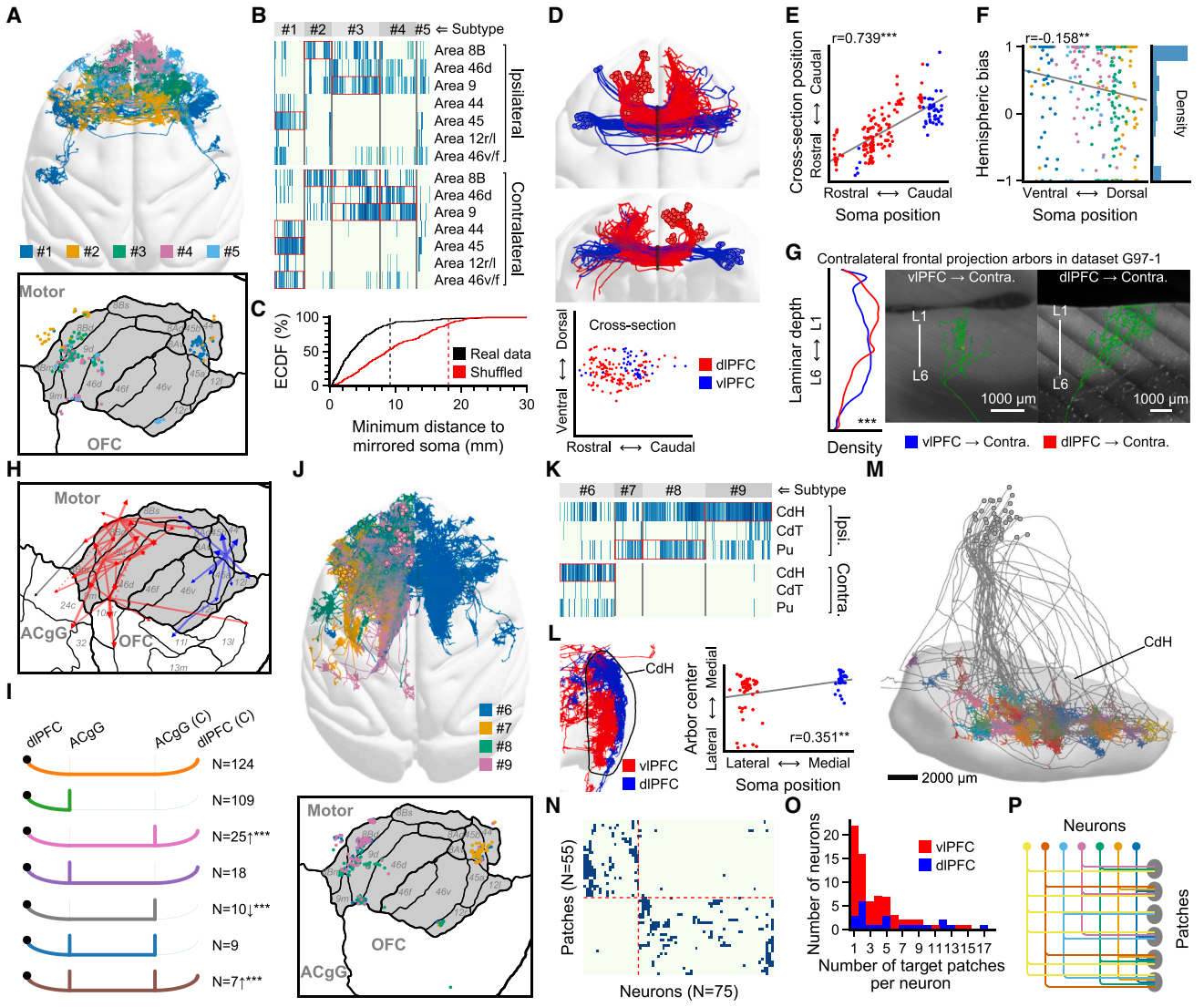

Figure 5. Contralateral and cortico-striatal projections of macaque PFC IT neurons

(A and B) Single-neuron projectomes, soma distributions, and projection targets of five ITc subtypes (#1–5).

(C) The ECDF of minimum distances between contralateral arbors and mirrored soma locations of ITc neurons.

(D and E) Axon trajectories and callosal bundle cross-section (D), and correlation between somata and callosal axon positions (E) for ITc neurons targeting contralateral homotypic regions.

(F) Hemispheric bias of ITc neurons correlated with soma positions.

(G) Laminar arborization patterns of contralateral arbors of dlPFC/vlPFC ITc neurons. Scale bars, 1,000 μm.

(H) Contralateral projections from dlPFC (red) and vlPFC (blue) ipsilateral subdomains to mirrored contralateral subdomains. Solid and dashed lines indicate the presence and absence of the projection to the corresponding ipsilateral subdomain, respectively.

(I) Projection patterns from dlPFC to contralateral homotypic and/or heterotypic targets, with significant deviations labeled.

(J and K) Single-neuron projectomes and soma distributions of four ITs subtypes (#6–9).

(L) Striatal arbor distributions and correlation between soma and arbor positions for dlPFC/vlPFC ITs neurons.

(M) Striatal arbor patches (randomly color-coded) in dataset G97-1. Scale bar, 2,000 μm.

(N) Projections from ITs neurons to striatal arbor patches for dlPFC/vlPFC neurons, respectively.

(O) Distribution of targeted arbor patch number in striatum per dlPFC/vlPFC neuron.

(P) Combinatorial innervation pattern from lPFC neurons to striatal patches.

For statistical significance, $^{**}p < 0.01$, $^{***}p < 0.001$.

Related to Figures S6.

Finally, we found that the contralateral projections originating from the dlPFC and vlPFC contained the highest proportion of type 3 arbors we defined (Figures 5G and S3G), consistent with the columnar terminal pattern of contralateral projections previously observed.[41]

We observed that some ITc neurons projected to heterotypic areas in the contralateral hemisphere. Similar to the ipsilateral projection map in Figure 4D, we constructed a contralateral projection map of PFC, which showed clear evidence for heterotypic projections (Figure 5H). Interestingly, for most (93.4%) heterotypic projections to contralateral subdomains, we could observe corresponding ipsilateral projections from the same source subdomains to the mirrored ipsilateral target subdomains (Figure 5H, arrows with solid line). We found that certain projection patterns, such as the co-projections to both contralateral homotypic and heterotypic areas, are enriched, while the projections only to contralateral heterotypic areas are under-represented. This is illustrated by the examples of bi-hemispheric projections of dlPFC neurons that targeted both dlPFC and ACgG in Figure 5I. Interestingly, when we considered striatum as a heterotypic target of ITc neurons in lPFC, the ITc projections to both the homotypic cortical area in contralateral lPFC and contralateral striatum were also enriched (Figure S6B). Thus, heterotypic projecting ITc neurons tended to co-innervate contralateral homotypic and heterotypic targets simultaneously.

We found that striatum-projecting ITs subtypes 7–9 projected solely to ipsilateral striatum, whereas subtype 6 predominantly projected to contralateral striatum in macaque (Figures 5J and 5K), suggesting these ITs subtypes are specialized for regulating either ipsilateral or contralateral striatum. Furthermore, ITs subtype 9 projected only to the head of caudate (CdH) within the striatum, whereas ITs subtypes 7 and 8 projected to both CdH and putamen (Pu) (Figure 5K). Within these areas, ITs neurons showed restricted topographic arborization, as dlPFC neurons arborized more medially in the striatum than vlPFC neurons (Figure 5L). Thus, macaque PFC ITs neurons followed a strict soma location-dependent topographic projection to striatum.

We found the presence of distinct arbor patches of ITs neurons in the dorsomedial striatum (Figure 5M), consistent with earlier studies of the patchy innervation in the striatum.[42,43] These orderly aligned arbor patches were formed by vlPFC neurons with somata intermixed within a local region in area 45. The average size of patches formed in the striatum (diameter 1.14 ± 0.10 mm, standard error of the mean [SEM], n = 12; see STAR Methods) was slightly larger than the average striatal arbor size (diameter 0.85 ± 0.02 mm, SEM, n = 781 arbors; see STAR Methods) of PFC ITs neurons. Moreover, most ITs PFC neurons arborized in multiple arbor patches in a combinatorial manner in the striatum (Figures 5N–5P), indicating a many-to-many wiring rule of PFC neurons innervating multiple arbor patches. Similar IT neuronal arbor patches composed of columnar arbors were also observed in the contralateral cortex (Figures S6C and S6D; see STAR Methods), with a patch size of 543 ± 45 μm (SEM, n = 7 contralateral patches), as illustrated in Figure S6E (top and bottom left), close to the patches of size 300–750 μm observed by Goldman-Rakic et al.[41] More generally, we found the average contralateral arbor size as 916 ± 17 μm (SEM, n = 1,243 arbors; see STAR Methods). We noted that some contralateral arbor patches can extend to stripes up to 7 mm long, as shown by the example stripe in area 45 in Figure S6E (bottom right). Together, our findings now provide comprehensive data on the arbor organization of the patches formed by various single IT neurons.

Subcortical projections of PFC neurons

In macaque, we found that PT neurons (Figure 6A, top and bottom left; Figure 6B) in PFC projected to numerous subcortical targets, including mediodorsal thalamus (MD), superior colliculus (SC), ventral tegmental area (VTA), substantia nigra (SN), and periaqueductal gray (PAG) in midbrain; pallidum (Pd) in basal ganglia; lateral hypothalamus (LHy) in hypothalamus; pontine nucleus (Pn); and locus coeruleus (LC) in pons, whereas CT neurons solely projected to the thalamus (Figure 6A, middle and bottom right; Figure 6C; Figure S7A). The projectome-defined PT neuron subtypes 11 and 12 were mainly located in dlPFC and vlPFC, respectively (Figure 6B), in which subtype 12 exhibited stronger projections to Pd and LHy compared with subtype 11. Since the primate lPFC projection to SC plays a crucial role in the cognitive control of visually guided saccades and goal-directed behavior,[44–46] we focused on SC projections of PT neurons. We found that dlPFC and vlPFC axons were highly segregated within the main axon trunks along the entire axon routes (Figure 6D), as indicated by high F_1 scores (see STAR Methods) (Figure 6E). Interestingly, such axon segregation was lost as axons left the axon bundles and branched into axon collaterals and terminal arbors at various locations along the main trunks toward SC. However, the soma location-dependent topography in the terminal arbors was regained in SC (Figures 6F and 6G, left), leading to differential distribution of axon arbors of dlPFC and vlPFC PT neurons in the medial and ventral parts of the SC, respectively. In addition, the terminal axons of dlPFC (Figure 6G, middle) and vlPFC (Figure 6G, right) were mainly distributed in the intermediate layer of SC (SCi), with some axons of dlPFC neurons also extending to the deep layer of SC (SCd). Interestingly, although vlPFC PT neurons were localized to a small PFC region, fine-grained soma-dependent topography could still be found within both the axon bundle and terminal arbors of dlPFC PT neurons (Figures S7B and S7C). Together, we have unveiled the organization rules for the main axons within axon fiber bundles, axon collaterals, and terminal arbors in subcortical target areas of PFC PT neurons at the single-neuron level.

The projections from PFC to MD, related to learning, memory, and decision-making,[47,48] are shown by our single-neuron projectomes of PFC CT neurons in macaque (Figure 6H). Besides MD, CT neurons also projected to the ventral anterior (VA) thalamus. Our projectome analyses revealed that subtype 10 of CT neurons projected to MD with a soma location-dependent axon topography at the single-neuron level. The topographic segregation between dlPFC and vlPFC CT neurons gradually declined along the axon trunk bundles, but the segregation was substantially restored at the targeted thalamic area (Figure 6I), resulting in a significant correlation between soma location in PFC along the mediolateral axis and axon arbor center location in MD along its thalamic dorsoventral axis (Figure 6J). This topographic organization is further illustrated by the distinct preferential distribution of terminal arbors within MD (Figure 6K).

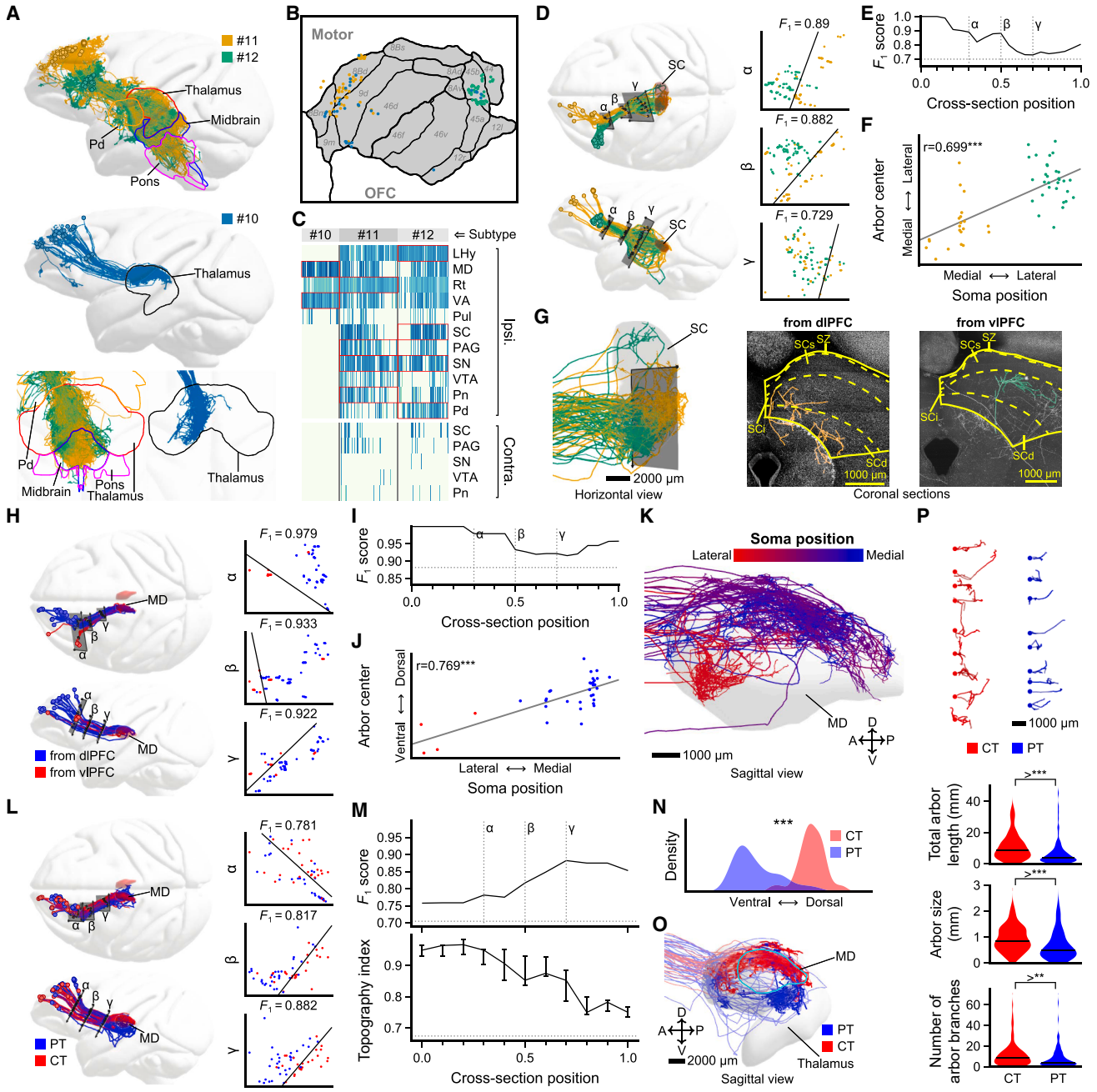

Figure 6. Cortico-subcortical projections of macaque PFC PT/CT neurons

(A–C) Single-neuron projectomes, soma distribution, and projection patterns of PT (#11–12) and CT (#10) subtypes.

(D–G) Axon trajectories with bundle cross-sections labeled (D), dlPFC-vlPFC bundle segregation quantified by F_1 scores (E), correlation between soma locations and arbor centers (F), and axonal distributions in SC (G) for the SC-targeted PT neurons. Scale bars in (G), 2,000 μm for the left panel and 1,000 μm for the right two panels. In (G), SZ, stratum zonale; SCs, superficial layer of SC; SCi, intermediate layer of SC; SCd, deep layer of SC.

(H–K) Axon trajectories with bundle cross-sections labeled (H), dlPFC-vlPFC bundle segregation quantified by F_1 scores (I), correlation between soma locations and arbor centers (J), and axonal distributions in MD (K) for CT neurons. Scale bar in (K), 1,000 μm.

(L–P) Axon trajectories with bundle cross-sections labeled (L), segregation and branching topography of PT and CT bundles (M), density distribution of thalamic arbors (N), sagittal view in thalamus (O), and morphological comparisons of axon terminal arbors (P) between CT and PT neurons. The line and bars of topography index in (M) indicate the 0.25, 0.5, and 0.75 quantiles. Scale bar in (O), 2,000 μm. The black lines in the violin plots of (P) indicate median values.

For the orientation indicators in (K) and (O), A, anterior; P, posterior; D, dorsal; V, ventral. For statistical significance, $^{**}p < 0.01$, $^{***}p < 0.001$.

Related to Figures S7.

While both PT and CT neurons projected to the thalamus, we found their projections showed clear preference for the ventral and dorsal thalamus, respectively (Figures 6L–6O). In particular, CT axons were mostly concentrated in MD, whereas PT axons broadly targeted other thalamic regions including midline, reticular, and ventral thalamus (Figures 6C and 6L). Interestingly, we found that the main axons of PT and CT neurons were traveling in the same axon bundle but became segregated in their collateral branches and terminal arbors toward the thalamus (Figure 6M), indicating that the neuron type (PT vs. CT) primarily determined the collateral branching toward specific thalamic targets (Figures 6N and 6O). Finally, we found that the terminal arbors of PT and CT neurons in the thalamus were clearly segregated and exhibited distinct arbor morphology (Figure 6P, top), with the size (average diameter) and strength (average total lengths) of the arborization much larger for CT axons as compared with PT axons (Figure 6P, bottom). Therefore, although both CT and PT neurons project to the thalamus via shared axon bundles, their collateral branches, projection targets, and arborization patterns were clearly different.

Comparison of macaque and mouse PFC projectomes

The PFC exhibits notable differences between primates and rodents.[49] For example, the dlPFC in macaque is distinguished by an extensive layer 3 and a well-defined layer 4, structural features that are absent in the mouse PFC,[50,51] and mouse medial PFC is organized differently from that of primates.[52,53] To uncover both shared and species-specific organizational principles, we have focused on the comparison of the long-range cortical and subcortical projections of PFC neurons and their morphological characteristics between macaque and mouse.

Comparison of long-range cortical projections of IT neurons

Comparing long-range cortical targets of macaque and mouse PFC IT neurons, we first identified their shared targets, including retrosplenial cortex (RSC), LIP, and temporal cortex in macaques, corresponding to retrosplenial area (RSP), posterior parietal association areas (PTLp), and temporal association area (TEa) in mice, respectively. We then examined the projections to these cortical targets in both macaque and mouse PFC IT neurons. We found that the topographic projections of macaque dlPFC and vlPFC IT neurons to RSC (subtype 32) vs. LIP (subtype 15) (Figure 3J) are similar to those of mouse neurons in the ventrolateral part (ORBvl) and lateral part (ORBl) of the orbital area projecting to RSP vs. PTLp (Figures 7A and 7B). In addition, temporal cortex-projecting (TEa-projecting) neurons can also be found in mouse ORBvl and ORBl, similar to the situation in macaque dlPFC/vlPFC. However, while mouse IT neurons exhibited substantial joint projections to RSP, PTLp, and TEa, macaque dlPFC/vlPFC IT neurons mostly projected to only one of these cortical targets (Figure 7C). Mouse neurons projecting to RSP and/or PTLp also tended to project to the primary visual cortex (VISp/V1), whereas the corresponding macaque neurons lacked this direct projection (Figure 7D), suggesting that intermediate relay of top-down signals is needed along the cortical hierarchy in the primate brain. Finally, we found similar laminar distributions of terminal arborization in TE (TEa) and LIP (PTLp) but different patterns for RSC (RSP) between the two species (Figures 7E and S7D). Therefore, we have identified shared gradients in the soma-target topography of cortical IT neurons between mouse and macaque PFC and found that macaque PFC IT neurons exhibited higher specificity in their cortical targeting than those in mice.

Comparison of contralateral projections of IT neurons

We then examined the proportions of IT neurons of macaque dlPFC/vlPFC and mouse ORBvl/ORBl exhibiting contralateral projection. We found that percentage of IT neurons projecting to the contralateral hemisphere was much lower in macaques (20%) than in mice (74%) (Figure 7F, left). For bilaterally projecting neurons, the hemispheric bias index for each neuron was significantly biased toward contralateral in macaques (median 0.55) than mice (median 0.20) (Figure 7F, right). Comparing the laminar distributions of terminal arborization between mouse and macaque PFC ITc neurons, we found that mouse arbors extend more preferentially to superficial layer in the contralateral cortex than macaque arbors (Figure S7E). Similar biases toward either ipsilateral or contralateral striatum were also found for macaque ITs neurons (Figure 7G), implicating that macaque bilaterally projecting neurons are more dedicated to the contralateral hemisphere. Therefore, macaque IT neurons are more specialized in their ipsilateral vs. contralateral projections than mouse IT neurons.

Comparison of subcortical projections of PT and CT neurons

We found that PT neurons in both macaque dlPFC/vlPFC and mouse ORBvl/ORBl projected to a similar set of target areas in the thalamus, pons, and midbrain, including VTA, SN, SC, and PAG (Figure 7H), and that CT neurons in both macaques and mice projected to MD in the thalamus. However, at the single-neuron level, PT and CT macaque neurons projected to significantly fewer target regions than those in mice (Figure 7I). PT neurons in macaque PFC are more biased toward ipsilateral projections vs. contralateral projections than PT neurons in mouse PFC (Figure 7J, left). In particular, almost no macaque CT neurons exhibited contralateral projections, whereas mouse CT neurons showed extensive contralateral targeting (Figure 7J, right). However, by comparing the PT neurons in mouse ORBvl/ORBl with corresponding neurons in macaque dlPFC/vlPFC (Figure S7F), we found a conserved soma location-dependent arbor gradient in SC along the mediolateral axis (Figure 6F). Similarly, the specific projections of CT neurons to MD were also conserved, with a shared soma location-dependent topography along the same mediolateral axis in both species (Figures 6J and S7G). Taken together, in comparison with mouse PFC neurons, macaque PFC PT and CT neurons have substantially reduced the number of targets, while the soma location-dependent topography in their arbor distribution in the subcortical targets was conserved.

General features of axon morphology of macaque and mouse PFC projection neurons

We first examined the number of axon branches and the total axon length of IT, PT, and CT neurons in macaque and mouse PFC projection neurons. Our analysis revealed that mouse IT neurons exhibited a significantly higher number (239 ± 3, SEM, n = 3,744 neurons) of branches over the entire axon than macaque IT neurons (140 ± 4, SEM, n = 2,045 neurons), which

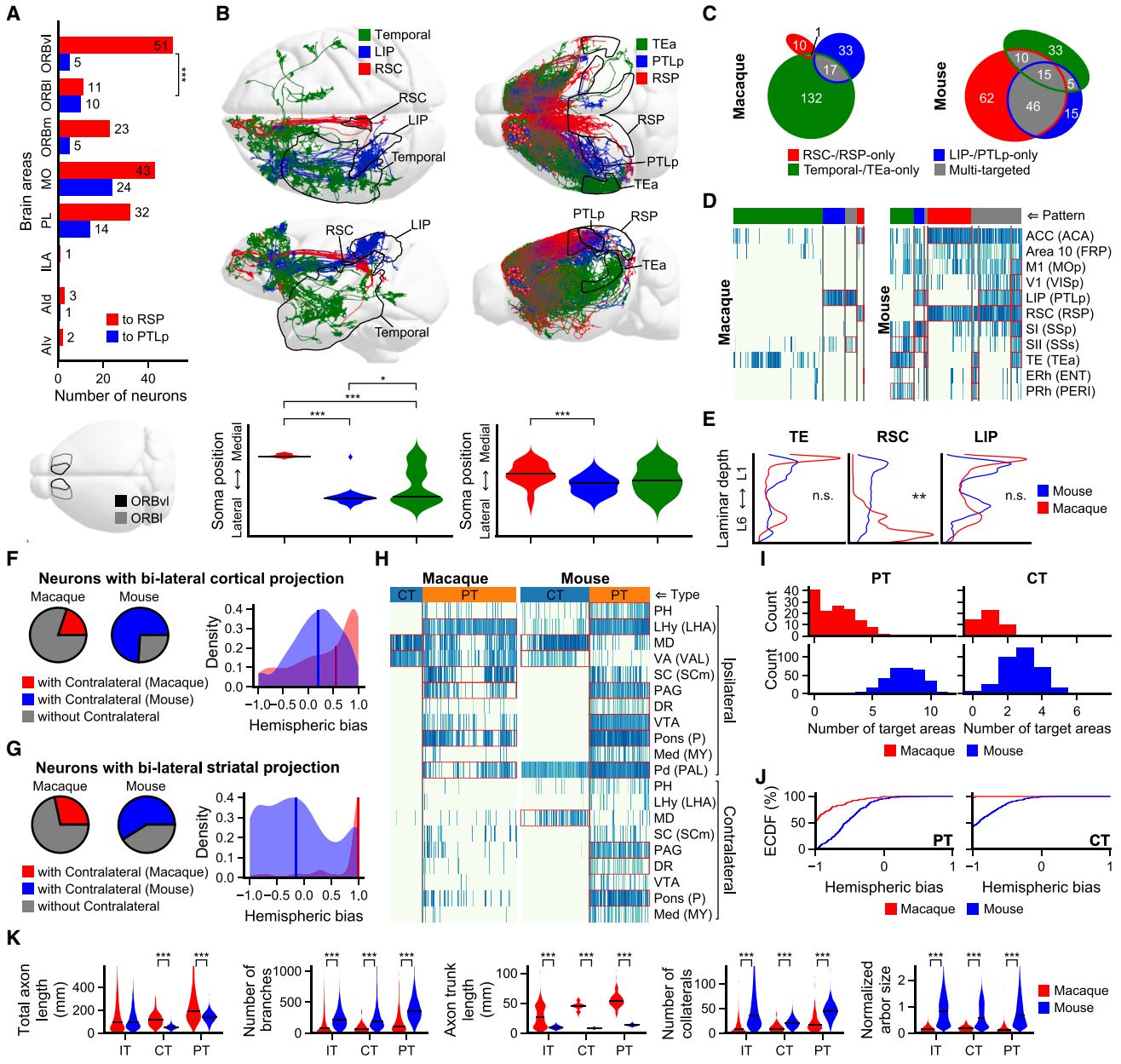

Figure 7. Comparison of PFC single-neuron projectomes between macaque and mouse

(A) Numbers of mouse neurons in different PFC subregions projecting to RSP and PTLp across subregions, with ORBvl and ORBl showing significant projection biases.

(B–E) Comparison of cortico-cortical projections of macaque and mouse PFC neurons, including mediolateral soma topography (B), the number of neurons projecting to three shared targets (C), projection patterns to distinct shared targets (D), and differential laminar distributions of axon arbors (E). The median soma positions are labeled with black lines for the violin plots of (B).

(F and G) Comparison of proportions and hemispheric biases of IT neurons with contralateral cortical (F) and striatal (G) projections in macaque and mouse. The median hemispheric bias values are labeled with blue/red lines in the right plots of (F) and (G).

(H–J) Comparison of PT/CT neuron projections, including projection patterns to shared targets (H), number of targeted regions per neuron (I), and hemispheric biases in subcortical projections assessed by ECDF (J).

(K) Comparison of axonal morphological features of IT, PT, and CT neurons. The median values are labeled with black lines in the violin plots.

For statistical significance, n.s., not significant; $^{*}p < 0.05$, $^{**}p < 0.01$, $^{***}p < 0.001$.

Related to Figures S7 and S8.

was also true for PT and CT neurons (Figure 7K). Surprisingly, the total axon lengths of single macaque IT neurons (135.8 ± 3.0 mm, SEM, n = 2,045) were close to those of single mouse IT neurons (122.8 ± 1.4 mm, SEM, n = 3,744), and this was found also for PT and CT neurons (Figure 7K). Although the average main axon trunk length was significantly longer in macaque neurons, as expected based on their brain size (Figure 7K), the number of collateral branches of macaque neurons was much lower than that of mouse neurons (Figure 7K). Furthermore, we found that the average arbor size in macaque IT neurons (0.824 ± 0.004 mm; SEM, n = 16,168 arbors) was very close to that of mouse IT neurons (0.902 ± 0.003 mm; SEM, n = 33,404 arbors). Given that the brain size of macaque is about 5 times larger than mouse brain, the arbor size normalized by brain size in macaques was substantially smaller than that in mice for IT, PT, and CT neurons (Figure 7K). Thus, there is a general reduction of collateral branch number and the relative size of axon arbors at the target zone from mice to macaques, implicating a higher spatial specificity and precision of macaque axon arborization at the target area. Finally, we have also identified differences in other morphological features such as fractal dimension and partition asymmetry between macaque and mouse IT, PT, and CT neurons (Figure S8). All of these structural features are likely to be important for the organization of neural networks in the primate brain.

DISCUSSION

In this study, large-scale automatic axon reconstruction combined with human collaborative proofreading yielded the whole-brain map for 2,231 single axons of PFC neurons in the macaque brain. Unbiased classification of single-neuron projectomes obtained 32 neuron subtypes, each of which could be associated with specific cognitive functions. Systematic comparison of single-neuron projectomes of macaque PFC with mouse PFC projectomes reported previously[11] revealed that each macaque PFC neuron mostly projected to a single target area, unlike the multi-targeting of mouse neurons. Most strikingly, we found that the total axon length, including the main axon trunk, collateral branches, and terminal arbors, in macaques is similar to that in mice, but the number of axon collaterals and axon arbor size relative to the brain size at the target areas was much smaller in macaques. Since the axon trunk increases greatly with the expansion of brain size in the macaque, we propose that the conservation of the total axon length due to intrinsic cellular constraints leads to the global reduction of axon collaterals and arborization of macaque neurons, suggesting the distinct organization for primate PFC projection neurons.

Primate brains possess structural and functional features that are distinct among mammals, reflecting their evolutionary trajectory and cognitive capabilities. In particular, cortico-cortical and cortico-striatal axon arbors tend to form patches in the primate brain. Our data showed that contralateral cortical axonal patches mainly consist of columnar axon arbors of restricted sizes, extending previous results by Goldman-Rakic and Schwartz[41] and providing the cellular basis of patch formation in the cortex. Patchy prefrontal inputs to the striatum have also been observed previously.[42,43] Our single-axon reconstruction further unraveled the many-to-many relationship between axon and patches in the striatum and a topographic order that depends on the soma location in PFC. Since the axon arbor size does not increase significantly as brain size expands from mice to macaques, the relative spatial coverage of the arbors at the target area is thus reduced, leading to more selective and refined targeting. Such highly structured organization can serve as a computational template for effective redistribution and combinatorial processing of PFC-striatal inputs that serve for context-dependent behavioral planning.[42]

The differences in neuronal architecture, connectivity efficiency, and cognitive processing between primates and non-primate species have been described.[54] The cortical connectivity in primates, marked by functional segregation, precise axonal projections, and hierarchical regulation, is crucial in shaping higher cognitive functions. Results of our cross-species comparison of single-neuron projectomes support the notion that primate evolution involves the emergence of highly modular and selective PFC networks. Unlike the mouse PFC neuron that sends projections to multiple targets, each macaque PFC neuron typically projects only to a single target, thus minimizing crosstalk between functionally distinct areas and ensuring greater accuracy in information transmission. Since the primate brain highly relies on top-down signaling from PFC to sensory and motor systems, the fine-tuned projection patterns we observed may enable focused attention to relevant stimuli, flexible cognitive control, and precise action selection, all of which are fundamental to executive functions.

Limitations of the study

There are several limitations in this study. First, the number of neurons with fully reconstructed projectomes remains limited. The characteristics of a particular projectome subtype we observed may be biased due to limited sampling. Since the viral infection efficiency was variable across experiments, the number of labeled cells at various injection sites was often variable. Second, the distribution of injection sites still covered a limited portion of the entire macaque PFC. Our effort to maximize the yield of labeled neurons per injection often resulted in neurons whose axons could not be traced back to their somata. Although these neurons could not be used in analyzing the precise soma location, they were used for studying axon branching and arborization. Third, as only female macaques were used in this study, potential sexual dimorphic differences in projectomes were not examined in this study. Finally, since our single-neuron macaque projectomes were pooled from seven different monkey brains, individual variations could compromise the spatial precision in cell registration to the reference macaque atlas. Future studies, including reconstruction of more neurons in the PFC, together with transcriptomic and functional analyses, will provide a more comprehensive single-cell mapping of the macaque brain.

RESOURCE AVAILABILITY

Lead contact

Further information and requests for resources should be directed to and will be fulfilled by the lead contact, Jun Yan (junyan@ion.ac.cn).

Materials availability

All the recombinant viruses used for Cre expression and fluorescent labeling in this study are commercially available.

Data and code availability

The reconstructed neurons are provided as SWC files at https://zenodo.org/records/15128612, and the web-based visualization of reconstructed neuron data is available at https://macaque.digital-brain.cn/projectome/pfc. The raw fMOST imaging datasets, due to their huge size, are available upon request. The software for neuron reconstruction is available in our previously published paper.[16] The Julia code for analysis is available at https://zenodo.org/records/15529826.

ACKNOWLEDGMENTS

This paper is from the Mesoscopic Brain Mapping Consortium. This work was supported by the National Science and Technology Innovation 2030 Major Program (STI2030-2021ZD0200100, 2021ZD0200204, 2021ZD0204400, 2021ZD0200104, and 2021ZD0201001), the Lingang Laboratory grant (LG202104-01-06), the National Science Foundation for Young Scientists of China grant (32300943), the National Key R&D Program of China (2020YFE0205900), and the CAS Project for Young Scientists in Basic Research (YSBR-116). We thank Dr. Rui Xu in Dr. Robert Desimone's lab at Massachusetts Institute of Technology (MIT) for providing the original fMRI data of the microstimulation experiment in lPFC. We thank Zhi Zeng and his team (Chengdu Huizhong Tianzhi Technology Co. Ltd) for manual proofreading using Gapr in this study. We thank the Center for Data and Computing in Brain Science (CDCBS) at the CAS Center for Excellence in Brain Science and Intelligence Technology for developing the web-based visualization of macaque PFC single-neuron projectome data in this study.

AUTHOR CONTRIBUTIONS

Design of the study and scientific direction: J.Y., C. Xu, Z.S., X.Y., Z.L., Q.L., and M.-m.P.; monkey surgery and virus injection: M.W., Q.C., J.F., and Z.S.; project coordination, virus preparation, and animal ethics: L.Z., X.S., and C. Xu; fMOST imaging: T.J., W.R., M.R., X.J., C. Xiao, A.L., X.L., Q.L., and X.Y.; data analysis: Gapr reconstruction of single neurons, L. Gou and Y.W.; single-neuron projectome analysis, L. Gou and Y.W.; functional interpretation: G.O. and T.Y.; comparative analysis of monkey and mouse projectomes, L. Gou, Y.W., L. Gao, and S.L.; interpretation and generation of figures, L. Gou, Y.W., J.Y., and M.-m.P.; writing, reviewing, and editing the manuscript: J.Y., M.-m.P., L. Gou, Y.W., G.O., and T.Y.; funding: J.Y., C. Xu, Z.S., X.Y., and Z.L.

DECLARATION OF INTERESTS

The authors declare no competing interests.

STAR★METHODS

Detailed methods are provided in the online version of this paper and include the following:

- KEY RESOURCES TABLE
- EXPERIMENTAL MODEL AND STUDY PARTICIPANT DETAILS
  - Animals
- METHOD DETAILS
  - MRI localization of brain regions
  - Single-neuron labeling by viral injection
  - Postoperative recovery and tissue collection
  - fMOST imaging
- QUANTIFICATION AND STATISTICAL ANALYSIS
  - Image data conversion & auto-reconstruction
  - Collaborative proofreading & quality control
  - Image block stitching & atlas registration
  - Identification of neuron types and subtypes
  - Analysis of subtype functions
  - Determination of cortical laminar depth
  - Comparison with population tracing
  - Segmentation of axon arbors
  - General arbor features
  - Laminar distribution of arbors
  - Detection of arbor patches
  - Identification of intra-PFC subdomains
  - Homo-/hetero-typic projection identification
  - Co-innervation analysis of PFC ITi neurons
  - Calculation of F_1 scores along axon routes
  - Topography index calculated along axon path
  - Definition of hemispheric bias index
  - Statistics

SUPPLEMENTAL INFORMATION

Supplemental information can be found online at https://doi.org/10.1016/j.cell.2025.06.005.

Received: December 23, 2024
Revised: April 10, 2025
Accepted: June 3, 2025
Published: July 10, 2025

REFERENCES

1. Murray, J.D., and Constantinidis, C. (2024). The Position of the Prefrontal Cortex in the Cortical Hierarchy. In The Frontal Cortex: Organization, Networks, and Function, S.N.H. Marie, T. Banich, and T.W. Robbins, eds. (The MIT Press) https://doi.org/10.7551/mitpress/15679.003.0009.
2. Goldman-Rakic, P.S. (2011). Circuitry of primate prefrontal cortex and regulation of behavior by representational memory. Compr. Physiol, 373–417. https://doi.org/10.1002/cphy.cp010509.
3. Levy, R., and Goldman-Rakic, P.S. (2000). Segregation of working memory functions within the dorsolateral prefrontal cortex. Exp. Brain Res. *133*, 23–32. https://doi.org/10.1007/s002210000397.
4. Mante, V., Sussillo, D., Shenoy, K.V., and Newsome, W.T. (2013). Context-dependent computation by recurrent dynamics in prefrontal cortex. Nature *503*, 78–84. https://doi.org/10.1038/nature12742.
5. Siegel, M., Buschman, T.J., and Miller, E.K. (2015). Cortical information flow during flexible sensorimotor decisions. Science *348*, 1352–1355. https://doi.org/10.1126/science.aab0551.
6. Crittenden, B.M., and Duncan, J. (2014). Task difficulty manipulation reveals multiple demand activity but no frontal lobe hierarchy. Cereb. Cortex *24*, 532–540. https://doi.org/10.1093/cercor/bhs333.
7. Markov, N.T., Ercsey-Ravasz, M.M., Ribeiro Gomes, A.R., Lamy, C., Magrou, L., Vezoli, J., Misery, P., Falchier, A., Quilodran, R., Gariel, M.A., et al. (2014). A weighted and directed interareal connectivity matrix for macaque cerebral cortex. Cereb. Cortex *24*, 17–36. https://doi.org/10.1093/cercor/bhs270.
8. Watakabe, A., Skibbe, H., Nakae, K., Abe, H., Ichinohe, N., Rachmadi, M. F., Wang, J., Takaji, M., Mizukami, H., Woodward, A., et al. (2023). Local and long-distance organization of prefrontal cortex circuits in the marmoset brain. Neuron *111*, 2258–2273.e10. https://doi.org/10.1016/j.neuron.2023.04.028.
9. Yan, M., Yu, W., Lv, Q., Lv, Q., Bo, T., Chen, X., Liu, Y., Zhan, Y., Yan, S., Shen, X., et al. (2022). Mapping brain-wide excitatory projectome of primate prefrontal cortex at submicron resolution and comparison with diffusion tractography. eLife *11*, e72534. https://doi.org/10.7554/eLife.72534.
10. Xu, R., Bichot, N.P., Takahashi, A., and Desimone, R. (2022). The cortical connectome of primate lateral prefrontal cortex. Neuron *110*, 312–327.e7. https://doi.org/10.1016/j.neuron.2021.10.018.
11. Gao, L., Liu, S., Gou, L., Hu, Y., Liu, Y., Deng, L., Ma, D., Wang, H., Yang, Q., Chen, Z., et al. (2022). Single-neuron projectome of mouse prefrontal

cortex. Nat. Neurosci. *25*, 515–529. https://doi.org/10.1038/s41593-022-01041-5.

12. Gao, L., Liu, S., Wang, Y., Wu, Q., Gou, L., and Yan, J. (2023). Single-neuron analysis of dendrites and axons reveals the network organization in mouse prefrontal cortex. Nat. Neurosci. *26*, 1111–1126. https://doi.org/10.1038/s41593-023-01339-y.
13. Liu, S., Gao, L., Chen, J., and Yan, J. (2024). Single-neuron analysis of axon arbors reveals distinct presynaptic organizations between feedforward and feedback projections. Cell Rep. *43*, 113590. https://doi.org/10.1016/j.celrep.2023.113590.
14. Zhou, C., Yang, X., Wu, S., Zhong, Q., Luo, T., Li, A., Liu, G., Sun, Q., Luo, P., Deng, L., et al. (2022). Continuous subcellular resolution three-dimensional imaging on intact macaque brain. Sci. Bull. (Beijing) *67*, 85–96. https://doi.org/10.1016/j.scib.2021.08.003.
15. Xu, F., Shen, Y., Ding, L., Yang, C.Y., Tan, H., Wang, H., Zhu, Q., Xu, R., Wu, F., Xiao, Y., et al. (2021). High-throughput mapping of a whole rhesus monkey brain at micrometer resolution. Nat. Biotechnol. *39*, 1521–1528. https://doi.org/10.1038/s41587-021-00986-5.
16. Gou, L., Wang, Y., Gao, L., Zhong, Y., Xie, L., Wang, H., Zha, X., Shao, Y., Xu, H., Xu, X., et al. (2024). Gapr for large-scale collaborative single-neuron reconstruction. Nat. Methods *21*, 1926–1935. https://doi.org/10.1038/s41592-024-02345-z.
17. Gou, L., Wang, Y., and Yan, J. (2025). Single-neuron projectomes of macaque prefrontal cortex reveal refined axon targeting and arborization. Zenodo. https://doi.org/10.5281/zenodo.15128612.
18. Jung, B., Taylor, P.A., Seidlitz, J., Sponheim, C., Perkins, P., Ungerleider, L.G., Glen, D., and Messinger, A. (2021). A comprehensive macaque fMRI pipeline and hierarchical atlas. Neuroimage *235*, 117997. https://doi.org/10.1016/j.neuroimage.2021.117997.
19. Seidlitz, J., Sponheim, C., Glen, D., Ye, F.Q., Saleem, K.S., Leopold, D.A., Ungerleider, L., and Messinger, A. (2018). A population MRI brain template and analysis tools for the macaque. Neuroimage *170*, 121–131. https://doi.org/10.1016/j.neuroimage.2017.04.063.
20. Gerfen, C.R., Economo, M.N., and Chandrashekar, J. (2018). Long distance projections of cortical pyramidal neurons. J. Neurosci. Res. *96*, 1467–1475. https://doi.org/10.1002/jnr.23978.
21. Harris, K.D., and Shepherd, G.M.G. (2015). The neocortical circuit: themes and variations. Nat. Neurosci. *18*, 170–181. https://doi.org/10.1038/nn.3917.
22. Ungerleider, L.G., Gaffan, D., and Pelak, V.S. (1989). Projections from inferior temporal cortex to prefrontal cortex via the uncinate fascicle in rhesus monkeys. Exp. Brain Res. *76*, 473–484. https://doi.org/10.1007/BF00248903.
23. Romanski, L.M., Tian, B., Fritz, J., Mishkin, M., Goldman-Rakic, P.S., and Rauschecker, J.P. (1999). Dual streams of auditory afferents target multiple domains in the primate prefrontal cortex. Nat. Neurosci. *2*, 1131–1136. https://doi.org/10.1038/16056.
24. Andrews-Hanna, J.R., Smallwood, J., and Spreng, R.N. (2014). The default network and self-generated thought: component processes, dynamic control, and clinical relevance. Ann. N. Y. Acad. Sci. *1316*, 29–52. https://doi.org/10.1111/nyas.12360.
25. Buckner, R.L., Andrews-Hanna, J.R., and Schacter, D.L. (2008). The brain's default network: anatomy, function, and relevance to disease. Ann. N. Y. Acad. Sci. *1124*, 1–38. https://doi.org/10.1196/annals.1440.011.
26. Selemon, L.D., and Goldman-Rakic, P.S. (1988). Common cortical and subcortical targets of the dorsolateral prefrontal and posterior parietal cortices in the rhesus monkey: evidence for a distributed neural network subserving spatially guided behavior. J. Neurosci. *8*, 4049–4068. https://doi.org/10.1523/JNEUROSCI.08-11-04049.1988.
27. Bisley, J.W., and Goldberg, M.E. (2010). Attention, intention, and priority in the parietal lobe. Annu. Rev. Neurosci. *33*, 1–21. https://doi.org/10.1146/annurev-neuro-060909-152823.
28. Borra, E., Gerbella, M., Rozzi, S., and Luppino, G. (2011). Anatomical evidence for the involvement of the macaque ventrolateral prefrontal area 12r in controlling goal-directed actions. J. Neurosci. *31*, 12351–12363. https://doi.org/10.1523/JNEUROSCI.1745-11.2011.
29. Gerbella, M., Belmalih, A., Borra, E., Rozzi, S., and Luppino, G. (2010). Cortical connections of the macaque caudal ventrolateral prefrontal areas 45A and 45B. Cereb. Cortex *20*, 141–168. https://doi.org/10.1093/cercor/bhp087.
30. Sakagami, M., and Pan, X. (2007). Functional role of the ventrolateral prefrontal cortex in decision making. Curr. Opin. Neurobiol. *17*, 228–233. https://doi.org/10.1016/j.conb.2007.02.008.
31. McCormick, D.A., Shu, Y., Hasenstaub, A., Sanchez-Vives, M., Badoual, M., and Bal, T. (2003). Persistent cortical activity: mechanisms of generation and effects on neuronal excitability. Cereb. Cortex *13*, 1219–1231. https://doi.org/10.1093/cercor/bhg104.
32. Kritzer, M.F., and Goldman-Rakic, P.S. (1995). Intrinsic circuit organization of the major layers and sublayers of the dorsolateral prefrontal cortex in the rhesus monkey. J. Comp. Neurol. *359*, 131–143. https://doi.org/10.1002/cne.903590109.
33. Levitt, J.B., Lewis, D.A., Yoshioka, T., and Lund, J.S. (1993). Topography of pyramidal neuron intrinsic connections in macaque monkey prefrontal cortex (areas 9 and 46). J. Comp. Neurol. *338*, 360–376. https://doi.org/10.1002/cne.903380304.
34. Arion, D., Enwright, J.F., 3rd, Gonzalez-Burgos, G., and Lewis, D.A. (2024). Cell Type-Specific Profiles and Developmental Trajectories of Transcriptomes in Primate Prefrontal Layer 3 Pyramidal Neurons: Implications for Schizophrenia. Am. J. Psychiatry *181*, 920–934. https://doi.org/10.1176/appi.ajp.20230541.
35. Arnsten, A.F.T., and Datta, D. (2024). Characterizing the Most Vulnerable Prefrontal Cortical Neurons in Schizophrenia. Am. J. Psychiatry *181*, 861–864. https://doi.org/10.1176/appi.ajp.20240731.
36. Schwartz, M.L., and Goldman-Rakic, P.S. (1984). Callosal and intrahemispheric connectivity of the prefrontal association cortex in rhesus monkey: relation between intraparietal and principal sulcal cortex. J. Comp. Neurol. *226*, 403–420. https://doi.org/10.1002/cne.902260309.
37. Friedman, H.R., and Goldman-Rakic, P.S. (1994). Coactivation of prefrontal cortex and inferior parietal cortex in working memory tasks revealed by 2DG functional mapping in the rhesus monkey. J. Neurosci. *14*, 2775–2788. https://doi.org/10.1523/JNEUROSCI.14-05-02775.1994.
38. Schwartz, M.L., and Goldman-Rakic, P.S. (1982). Single cortical neurones have axon collaterals to ipsilateral and contralateral cortex in fetal and adult primates. Nature *299*, 154–155. https://doi.org/10.1038/299154a0.
39. Arion, D., Enwright, J.F., Gonzalez-Burgos, G., and Lewis, D.A. (2023). Differential gene expression between callosal and ipsilateral projection neurons in the monkey dorsolateral prefrontal and posterior parietal cortices. Cereb. Cortex *33*, 1581–1594. https://doi.org/10.1093/cercor/bhac157.
40. Zhou, J., Wen, Y., She, L., Sui, Y.N., Liu, L., Richards, L.J., and Poo, M.M. (2013). Axon position within the corpus callosum determines contralateral cortical projection. Proc. Natl. Acad. Sci. USA *110*, E2714–E2723. https://doi.org/10.1073/pnas.1310233110.
41. Goldman-Rakic, P.S., and Schwartz, M.L. (1982). Interdigitation of contralateral and ipsilateral columnar projections to frontal association cortex in primates. Science *216*, 755–757. https://doi.org/10.1126/science.6177037.
42. Eblen, F., and Graybiel, A.M. (1995). Highly restricted origin of prefrontal cortical inputs to striosomes in the macaque monkey. J. Neurosci. *15*, 5999–6013. https://doi.org/10.1523/JNEUROSCI.15-09-05999.1995.
43. Johnston, J.G., Gerfen, C.R., Haber, S.N., and van der Kooy, D. (1990). Mechanisms of striatal pattern formation: conservation of mammalian compartmentalization. Brain Res. Dev. Brain Res. *57*, 93–102. https://doi.org/10.1016/0165-3806(90)90189-6.
44. Borra, E., Gerbella, M., Rozzi, S., Tonelli, S., and Luppino, G. (2014). Projections to the superior colliculus from inferior parietal, ventral premotor,

and ventrolateral prefrontal areas involved in controlling goal-directed hand actions in the macaque. Cereb. Cortex *24*, 1054–1065. https://doi.org/10.1093/cercor/bhs392.

45. Koval, M.J., Lomber, S.G., and Everling, S. (2011). Prefrontal cortex deactivation in macaques alters activity in the superior colliculus and impairs voluntary control of saccades. J. Neurosci. *31*, 8659–8668. https://doi.org/10.1523/JNEUROSCI.1258-11.2011.
46. Lowe, K.A., Zinke, W., Cosman, J.D., and Schall, J.D. (2022). Frontal eye fields in macaque monkeys: prefrontal and premotor contributions to visually guided saccades. Cereb. Cortex *32*, 5083–5107. https://doi.org/10.1093/cercor/bhab533.
47. Browning, P.G.F., Chakraborty, S., and Mitchell, A.S. (2015). Evidence for Mediodorsal Thalamus and Prefrontal Cortex Interactions during Cognition in Macaques. Cereb. Cortex *25*, 4519–4534. https://doi.org/10.1093/cercor/bhv093.
48. Perry, B.A.L., Mendez, J.C., and Mitchell, A.S. (2023). Cortico-thalamocortical interactions for learning, memory and decision-making. J. Physiol. *601*, 25–35. https://doi.org/10.1113/JP282626.
49. Haber, S.N., and Robbins, T. (2022). The prefrontal cortex. Neuropsychopharmacology *47*, 1–2. https://doi.org/10.1038/s41386-021-01184-2.
50. Petrides, M., and Pandya, D.N. (1999). Dorsolateral prefrontal cortex: comparative cytoarchitectonic analysis in the human and the macaque brain and corticocortical connection patterns. Eur. J. Neurosci. *11*, 1011–1036. https://doi.org/10.1046/j.1460-9568.1999.00518.x.
51. Van De Werd, H.J., Rajkowska, G., Evers, P., and Uylings, H.B.M. (2010). Cytoarchitectonic and chemoarchitectonic characterization of the prefrontal cortical areas in the mouse. Brain Struct. Funct. *214*, 339–353. https://doi.org/10.1007/s00429-010-0247-z.
52. Wallis, C.U., Cardinal, R.N., Alexander, L., Roberts, A.C., and Clarke, H.F. (2017). Opposing roles of primate areas 25 and 32 and their putative rodent homologs in the regulation of negative emotion. Proc. Natl. Acad. Sci. USA *114*, E4075–E4084. https://doi.org/10.1073/pnas.1620115114.
53. Roberts, A.C. (2020). Prefrontal Regulation of Threat-Elicited Behaviors: A Pathway to Translation. Annu. Rev. Psychol. *71*, 357–387. https://doi.org/10.1146/annurev-psych-010419-050905.
54. Magrou, L., Joyce, M.K.P., Froudist-Walsh, S., Datta, D., Wang, X.J., Martinez-Trujillo, J., and Arnsten, A.F.T. (2024). The meso-connectomes of mouse, marmoset, and macaque: network organization and the emergence of higher cognition. Cereb. Cortex *34*, bhae174. https://doi.org/10.1093/cercor/bhae174.
55. Wang, Q., Ding, S.L., Li, Y., Royall, J., Feng, D., Lesnar, P., Graddis, N., Naeemi, M., Facer, B., Ho, A., et al. (2020). The Allen Mouse Brain Common Coordinate Framework: A 3D Reference Atlas. Cell *181*, 936–953. e20. https://doi.org/10.1016/j.cell.2020.04.007.
56. Scorcioni, R., Polavaram, S., and Ascoli, G.A. (2008). L-Measure: a web-accessible tool for the analysis, comparison and search of digital reconstructions of neuronal morphologies. Nat. Protoc. *3*, 866–876. https://doi.org/10.1038/nprot.2008.51.
57. Paxinos, G., Petrides, M., and Evrard, H.C. (2023). The Rhesus Monkey Brain in Stereotaxic Coordinates (Academic Press).
58. Ronneberger, O., Fischer, P., and Brox, T. (2015). U-Net: Convolutional Networks for Biomedical Image Segmentation (Springer), pp. 234–241.
59. Feng, L., Zhao, T., and Kim, J. (2015). neuTube 1.0: a new design for efficient neuron reconstruction software based on the SWC format. eNeuro *2*, ENEURO.0049-14.2014. https://doi.org/10.1523/ENEURO.0049-14.2014.
60. Huang, Y., and Huang, J.X. (2024). Exploring ChatGPT for next-generation information retrieval: Opportunities and challenges*22* (Sage Publications), pp. 31–44. https://doi.org/10.3233/WEB-230363.
61. Li, Q., Li, L., and Li, Y. (2024). Developing ChatGPT for biology and medicine: a complete review of biomedical question answering. Biophys. Rep. *10*, 152–171. https://doi.org/10.52601/bpr.2024.240004.
62. Liu, A., Feng, B., Wang, B., Wang, B., Liu, B., Zhao, C., Dengr, C., Ruan, C., Dai, D., and Guo, D. (2024). Deepseek-v2: A strong, economical, and efficient mixture-of-experts language model. Preprint at arXiv. https://doi.org/10.48550/arXiv.2405.04434.
63. Steele, G.E., and Weller, R.E. (1995). Qualitative and quantitative features of axons projecting from caudal to rostral inferior temporal cortex of squirrel monkeys. Vis. Neurosci. *12*, 701–722. https://doi.org/10.1017/S0952523800008981.
64. Yamashita, A., and Arikuni, T. (2001). Axon trajectories in local circuits of the primary motor cortex in the macaque monkey (Macaca fuscata). Neurosci. Res. *39*, 233–245. https://doi.org/10.1016/S0168-0102(00)00220-0.
65. Rockland, K.S. (1989). Bistratified distribution of terminal arbors of individual axons projecting from area V1 to middle temporal area (MT) in the macaque monkey. Vis. Neurosci. *3*, 155–170. https://doi.org/10.1017/S0952523800004466.
66. Rockland, K.S. (1992). Configuration, in serial reconstruction, of individual axons projecting from area V2 to V4 in the macaque monkey. Cereb. Cortex *2*, 353–374. https://doi.org/10.1093/cercor/2.5.353.
67. Parent, A., Charara, A., and Pinault, D. (1995). Single striatofugal axons arborizing in both pallidal segments and in the substantia nigra in primates. Brain Res. *698*, 280–284. https://doi.org/10.1016/0006-8993(95)01017-P.
68. Parent, M., and Parent, A. (2006). Single-axon tracing study of corticostriatal projections arising from primary motor cortex in primates. J. Comp. Neurol. *496*, 202–213. https://doi.org/10.1002/cne.20925.
69. Chen, A., Sun, Y., Lei, Y., Li, C., Liao, S., Meng, J., Bai, Y., Liu, Z., Liang, Z., Zhu, Z., et al. (2023). Single-cell spatial transcriptome reveals cell-type organization in the macaque cortex. Cell *186*, 3726–3743.e24. https://doi.org/10.1016/j.cell.2023.06.009.

STAR★METHODS

KEY RESOURCES TABLE

REAGENT or RESOURCE	SOURCE	IDENTIFIER
Bacterial and virus strains		
rAAV-CAG-DIO-EGFP-WPRE-hGH polyA	BrainVTA (Wuhan) Co., Ltd	Cat.No.PT-0168
rAAV-CAG-DIO-tdTomato-WPRE-hGH polyA	Brain Case Biotech Co., Ltd	Cat.No.BC-0870
rAAV-hSyn-SV40 NLS-Cre-WPRE-hGH polyA	Brain Case Biotech Co., Ltd	Cat.No.BC-0159
Biological samples		
#138 Cynomolgus monkey (6-year-old, 7.9 kg)	This study	N/A
#549 Cynomolgus monkey (9-year-old, 6.0 kg)	This study	N/A
#917 Cynomolgus monkey (9-year-old, 7.7 kg)	This study	N/A
#97 Cynomolgus monkey (8-year-old, 6.2 kg)	This study	N/A
#670 Cynomolgus monkey (8-year-old, 6.4 kg)	This study	N/A
#462 Cynomolgus monkey (13-year-old, 4.5 kg)	This study	N/A
#401 Cynomolgus monkey (12-year-old, 6.4 kg)	This study	N/A
Chemicals, peptides, and recombinant proteins		
Isoflurane	Hebei Jindafu Pharmaceutical Co., Ltd.	N/A
Atropine sulfate	Henan Runhong Pharmaceutical Co., Ltd.	N/A
Zoletil 50	VIRBAC	N/A
Lidocaine	Tongfang Pharmaceutical Group Co., Ltd.	N/A
Cefazolin	Suzhou Sino-Pharm Industrial Co., Ltd.	N/A
Dexamethasone	Chengxin Pharmaceutical Co., Ltd.	N/A
Meloxicam	Qilu Animal Health Products Co., Ltd.	N/A
Deposited data		
Mouse PFC neurons	Yan Lab; Gao et al.[11]	Mouse neuron visualization data: https://mouse.digital-brain.cn/projectome/pfc
NMT v2	Jung et al.[18]; Seidlitz et al.[19]	NMT v2 template data: https://afni.nimh.nih.gov/pub/dist/doc/htmldoc/nonhuman/macaque_tempatl/template_nmtv2.html
Allen CCF	Allen Brain Institute; Wang et al.[55]	Allen CCF template data: https://community.brain-map.org/t/allen-mouse-ccf-accessing-and-using-related-data-and-tools/359
Reconstructed neurons	This paper	Macaque neuron Zenodo data: https://zenodo.org/records/15128612
Web-based visualization of reconstructed neurons	This paper	Macaque neuron visualization data: https://macaque.digital-brain.cn/projectome/pfc
Software and algorithms		
Gapr (v1.1.0.11)	Yan Lab; Gou et al.[16]	http://yanlab.org.cn/gapr-en/
L-Measure (v5.3)	Sridevi Polavaram[56]	http://cng.gmu.edu:8080/Lm/
Julia (v1.11.2)	Julia	https://julialang.org/
Code for analysis	This paper	Zenodo data: https://zenodo.org/records/15529826

EXPERIMENTAL MODEL AND STUDY PARTICIPANT DETAILS

Animals

Brains in their entirety were collected from seven female cynomolgus monkeys (*Macaca fascicularis*). The basic information (sample ID, sex, weight, and date of birth) and the ethical approval numbers for each cynomolgus monkey are provided in Table S1.

The animal protocol was approved (Nos. CEBSIT-2020022 and CEBSIT-2022017) by the Biomedical Research Ethics Committee of the Center for Excellence in Brain Science and Intelligence Technology, Chinese Academy of Sciences. Animal care was conducted in accordance with the committee's guidelines.

METHOD DETAILS

MRI localization of brain regions

For experimental animals, MRI scanning was performed to visualize the brain. During the procedure, anesthesia was maintained using inhaled isoflurane (0.8%–1.5%), while heart rate and end-tidal CO_2 were monitored using a physiological monitoring system (SAII Model 1030 MR-compatible Small Animal Monitoring & Gating System), and body temperature was kept stable with a water-circulating heating system (Liangshanbo water heating main unit equipped with Walker durable non-woven water blanket). Whole-brain T1-weighted imaging was conducted using an MRI scanner (Siemens MAGNETOM Trio 3T) with a custom-built 8-channel surface coil. The MRI dates (date of performing MRI) for each cynomolgus monkey are listed in Table S1. After scanning, T1 structural images of the brain were obtained. Cortical regions were localized using the T1 MRI images in combination with a standard brain atlas.[57]

Single-neuron labeling by viral injection

To ensure the animals were in good health, they were observed the day before surgery for normal feeding, hydration, and general behavior. Food was withheld 8–12 hours before the surgery. On the day of surgery, monitoring and detection devices (e.g., monitors, heating blankets) were activated to confirm proper functioning. Atropine sulfate (0.02–0.08 mg/kg) was intramuscularly administered, followed by an intramuscular injection of Zoletil 50 (4–6 mg/kg) after 5–10 minutes for induction of anesthesia. After anesthesia induction, the animals were weighed and transferred to the surgical room. The cranial surgical area was shaved, and tracheal intubation was performed. The parameters of the ventilator were set based on body weight. Lidocaine ointment was applied to the intubation tube to minimize irritation. Anesthesia was maintained with inhaled isoflurane (1.5%–3%).

The animals were secured in the stereotaxic injection apparatus. The surgical site was cleaned with povidone-iodine and alcohol, and lidocaine ointment was applied to ear bars and eye hooks to reduce irritation. The incision site was identified based on the ear bar position, the skin was incised, and bleeding was controlled using electrocautery. After exposing the skull, the craniotomy site was marked based on MRI images (navigated by the BrainSight system of Rogue Research Inc.), and a craniotomy was performed using a surgical drill. Heart rate was continuously monitored, and anesthesia was increased as needed to reduce stimulation. After opening the dura mater, the injection needle was advanced to the target site while observing blood vessels with a stereomicroscope (Leica M320) to avoid damage.

At the designated brain regions, a stereotaxic injection syringe pump (Legato 130, Catalog No.788130) was used to perform viral injections. Virus tagged with fluorescent protein (rAAV-CAG-DIO-EGFP-WPRE-hGH polyA, titer: 4.57×10^{12} v.g./mL; or another virus rAAV-CAG-DIO-tdTomato-WPRE-hGH polyA, titer: 1.10×10^{13} v.g./mL) was 1:1 mixed with Cre virus (rAAV-hSyn-SV40 NLS-Cre-WPRE-hGH polyA, original titer: 1.05×10^{13} v.g./mL, with the final dilution factor 40000–80000 times after mixing). The final injection volume was 0.2–2 μL for each injection site. A micro-infusion pump (20–100 nL/min) was used to deliver the virus to the appropriate location. Information on the adeno-associated virus (AAV) and specific details of virus injection sites for each cynomolgus monkey (virus injection date, injected fluorescent-protein-sequence-tagged AAV, final dilution factor of Cre AAV, total volume of injection, and waiting time during AAV injection) are provided in Table S1.

After the injections, the exposed brain tissue was covered with artificial dura mater, and the craniotomy site was sealed with tissue glue and bone cement. The surface tissue was sutured. Animals were returned to their cages for observation after regaining consciousness. Postoperatively, antibiotics (cefazolin, 0.04–0.06 g/kg), dexamethasone (0.4–0.6 mg/kg), and analgesics (fentanyl citrate, 4–6 μg/kg; or Analgin, 0.2–0.5 mL/kg; or meloxicam, 0.1 mg/kg) were intramuscularly administered.

Postoperative recovery and tissue collection

Postoperative care addressed potential pain, elevated intracranial pressure, and infection risk. To alleviate pain, intramuscular administration of analgin (0.2–0.5 mL/kg) or meloxicam (0.1 mg/kg) was performed once daily for 3 days. Cefazolin (0.04–0.06 g/kg) was administered intramuscularly twice daily for 5–7 days to prevent infection. To reduce intracranial pressure, dexamethasone (0.4–0.6 mg/kg) was administered intramuscularly twice daily for 5–7 days. Animals with feeding difficulties received gavage feeding under veterinary guidance.

Two to three months after AAV injection, animals were euthanized. Anesthesia was induced using Zoletil 50 (4–6 mg/kg). In the perfusion room, deep anesthesia was achieved with an overdose (4–5 times the standard dose) of xylazine hydrochloride and Zoletil 50. After approximately 15 minutes, deep anesthesia was confirmed. Perfusion was performed sequentially with

PBS (0.6 L/kg) and paraformaldehyde (4% in PBS, 0.6 L/kg). The dates of perfusion for each cynomolgus monkey are listed in Table S1. The brain tissues were extracted after perfusion for the following fMOST imaging.

fMOST imaging

The image acquisition of the whole macaque brain basically follows the pipeline we developed in previous research.[14] The macaque brain was immersed in poly-N-acryloyl glycinamide hydrogel solution for 7 days before the polymerization. Then it was embedded in agarose for further imaging. The imaging was automatically performed using our fMOST system, which combined the high-precision large-scale vibratome and line-scan confocal microscope with the voxel size of $0.65\times0.65\times3$ μm^3. During the imaging, the surface of the sample with a thickness of 12 μm was removed with the microtome. Then four layers with the distance of 3 μm in depth were imaged in turn using the line-scan confocal microscope stripe-by-stripe. The position of the first imaging layer is 10 μm below the mechanical sectioning plane, to avoid the data loss induced by the sectioning. The imaging-sectioning cycles were performed from rostral to caudal of the macaque brain until all of the images of the brain were acquired. As the neurons were labeled with green fluorescent protein (GFP) and tdTomato, we adopted both green and red imaging channels to simultaneously acquire the images for them. After image acquisition, flat field correction and stitching were performed for stripe images to recover each image in the coronal plane of the brain. And the images were stored with Tagged Image File Format (TIFF) for further processing.

QUANTIFICATION AND STATISTICAL ANALYSIS

Image data conversion & auto-reconstruction

Gapr provides a highly efficient module (gapr-convert) for on-demand conversion of large-scale imaging datasets.[16] Imaging datasets were split into smaller cubes and were compressed to save on both storage and network bandwidth. Besides, only cubes that contain neuronal structures were converted with on-demand conversion. For example, a dataset originally sized of 432 TiB was compressed to about only 3.75 TiB (dataset G97-1). Furthermore, conversion begins immediately following a preliminary prescan, enabling reconstruction to proceed without waiting for the entire dataset to be processed (Figure 1B).

Gapr leverages deep learning for automatic neuron reconstruction. A 3-dimensional (3D) U-Net[58] was used to segment imaging data to predict the presence of neurite signals at voxel locations, which enhanced the accuracy of automatic reconstruction, particularly for faint signals. Then, the neuTube algorithm[59] was used to extract neurite skeletons, and the extraction process was performed iteratively for all overlapping cubes that contain neurite signals, covering datasets of virtually unlimited size.

The Gapr Gather module, as the hub for automatic reconstruction and collaborative manual proofreading, was deployed to a virtual network server that equipped with two cores (2.5 GHz Intel Xeon Platinum 8163 processor), 32 GiB of RAM, and 2 MiB/s bandwidth. The Gapr Convert module ran on a workstation featuring 16 cores (3.5 GHz Intel Xeon E5-1620 CPU), 104 GiB of RAM, and with connection to hard drives containing raw fMOST imaging data. Another Gapr Gather module instance was dedicated to managing image conversion and provided image access for reconstruction. The Trace module ran on a workstation featuring 16 cores (3.5 GHz Intel Xeon E5-2637 CPU), 128 GiB of RAM, and a dedicated GPU (NVIDIA GeForce GTX 1080 Ti).

Collaborative proofreading & quality control

Gapr can accommodate more than 100 people simultaneously performing real-time online reconstruction of single neurons. This pattern of collaborative reconstruction was reflected in the entire process of neuron reconstruction (Figure S1A), and this was supported by the Gapr Proofread and Fix modules running on standard desktop or laptop computers owned by the annotators. The images for neuron reconstruction were shared to annotators through the Internet, supported by the Center for Data and Computing in Brain Science (CDCBS) at the Center for Excellence in Brain Science and Intelligence Technology (CEBSIT), Chinese Academy of Sciences (CAS).

During the manual proofreading stage, annotators addressed unresolved issues by connecting segments missed by the automated algorithm, removing extraneous connections, and correcting incorrectly identified branches with the Proofread module. Particular attention was given to regions prone to errors, such as those around somata, dendritic branching points, and areas where many dendrite branches were in close proximity. While proofreading, neuron reconstruction errors came from mismatches between the imaging data and reconstruction results. Simple errors were fixed on the spot, but complex ones were sent to experts by labeling of error annotations. These error annotations were categorized (e.g., fixed, unresolved, deferred) and reviewed by experts to ensure the reconstruction accuracy. At the subsequent stage of single-neuron examination, experienced annotators ultimately resolved complex connectivity challenges and verified the reconstructed neurons with the Fix module. This manual review focused on ensuring the clarity of neurites in the images, confirming that significant errors compromising major branches were resolved, and cross-referencing known neuron morphology.

During neuron tracing, experienced annotators performed quality checks of reconstructed results at the same time. For further assurance of reconstruction precision, imaging cubes were randomly sampled to assess the quality of reconstruction after proofreading. As the gather module in Gapr logs a comprehensive reconstruction history, annotators who failed to resolve or report errors in the reconstruction process could be identified and held accountable for the corresponding tracing regions.

Image block stitching & atlas registration

For certain brain samples, fMOST imaging was performed on two or more separate sample blocks. For these samples, neuron reconstruction was performed separately for each continuous part of the whole volume. Afterwards, adjacent image blocks were stitched together, and disconnected parts of neurons that span multiple blocks were connected at block borders to produce complete axon tree structures. Various pieces of evidence were considered to connect axons at block borders:

coarse and precise correspondence of brain location based on the outlines of brain regions, blood vessels, and nearby neurites;
correspondence of neurite features including orientation, radius and brightness;
correspondence of relative position and neurite features of nearby neurites.

To ensure the correctness of axon stitching, cross-border connection of axons was applied only when it was plausible based on these considerations, and no other plausible alternatives of connection existed.

We used a custom Julia program to perform registration to the NMTv2 reference atlas[18,19] that integrates cross-border axon connection information. Firstly, a few manually picked landmarks were used to setup the preliminary affine transformation, establishing a coarse overlap between the sample and the reference. Then we refined registration by introducing a layer of non-rigid (BSpline) transformation and minimizing the pixel-wise difference between the transformed sample and the reference. Multi-block sample images were accepted, and concurrent registration of multiple blocks to the reference resulted in image stitching of the input sample blocks.

As the background fluorescence signal used for registration was different from the MRI imaging of the reference atlas, we used U-Net to produce MRI-like images, such that pixel-wise image difference was able to be calculated between the sample and the reference. The overall registration process can be summarized as:

$$\arg\min_{A,W,U} L(\text{Reference}, U \circ W \circ A(\text{Sample})),$$

where A and W are the affine and non-rigid transformations respectively, U is the U-Net, L is the loss function of image difference.

In our custom program, a batch of randomly sampled 2-dimensional (2D) images, instead of the whole volume, were used in each iteration of the stochastic gradient descent (SGD) minimizing process. The Flux machine learning framework of Julia was used for minimization.

Identification of neuron types and subtypes

Projection types of neurons were defined by manual inspection of reconstruction structures and regional distribution of axons in fMOST imaging results. According to the observed different projection patterns, we classified all neurons as IT, PT and CT neurons by the following criteria:

IT neurons project to cortical or striatal regions exclusively;
PT neurons project to mid-brain, hypothalamus, pons and/or medulla;
and CT neurons project to thalamic regions but not the typical targeted regions of PT neurons.

IT neurons were further classified into three subtypes by their different projection regions: ITi (projecting to ipsilateral cortex exclusively), ITs (projecting to striatum) and ITc (projecting to contralateral cortex). If both striatal and contralateral projections are both present, we classified these neurons as ITs neurons for the soma distribution and arbor distribution of most neurons are predominantly similar to ITs neurons.

Neuron subtypes are derived from clustering analysis of axon morphology. We first utilized the refined FNT-dist tool[11] in Gapr to calculate morphological dissimilarities between pairs of neurons. To ensure that each neuron subtype corresponds to only one neuron type (ITi, ITc, ITs, PT, CT), the distance between neurons of different types was increased by a constant value. Then, hierarchical clustering was performed on the resulting distance matrix with "ward_presquared" linkage. The dendrogram of hierarchical clustering was finally cut to produce 32 clusters, defining the 32 neuron subtypes in this study.

Analysis of subtype functions

Firstly, we summarized the projection patterns of neuron subtypes by identifying their soma locations, target regions, and projection laterality (bilateral, contralateral-only, or ipsilateral-only) (Table S2A). We utilized ChatGPT,[60,61] a large language model, to perform an artificial-intelligence-based (AI-based) literature retrieval for collecting functional information associated with relevant brain regions in our study. The consolidated biological functional annotations, after manual curation, are summarized in Table S2B. These biological functions were categorized into corresponding subcategories and broader functional categories (Table S2C).

Then, we determined the functional annotation for each PFC neuron (N_i) based on the congruency among the sets of function terms for both the PFC area where the soma was located (s_i) and its targeted brain areas (T_i). Let F_j denote the set of function terms for brain area j, the functional annotation for the neuron was calculated as $f^*(N_i) = \arg\min_f D(f, N_i)$ by minimizing

$$D(f, N_i) = \sum_{j \in \{s_i\} \cup T_i} w_{ij} \min_{g \in F_j} |f - g|.$$

Here, w_{ij} are weights and $|f - g|$ is the distance between the two function terms. As an example, if all relevant brain areas of a neuron share a common function term, this neuron is annotated by this common function term.

For the brain area where the soma was located, w_{is_i} is defined to be 1. For target areas, w_{ij} is proportional to the path distance to soma, and is normalized such that the most distant target (t_i^*) has $w_{it_i^*} = 1$.

The calculation of distance between function terms, $|f - g|$, was also assisted by the artificial intelligence (AI). With a local installation of DeepSeek R1 (32b version),[62] we provided a list of 32 randomly-selected function terms and asked the language model to group the terms by relevance and similarity, in the context of neuroscience terms. After over 200 such term grouping experiments, we calculated the distance between terms as one minus the probability of their co-occurrence in a group. For example, two terms that were never grouped together have a distance 1, and two closely related terms have a distance near zero.

Finally, we found predominant functions for each subtype by enrichment analysis. For a candidate function term and a neuron subtype, a Fisher's exact test with an alternative hypothesis that the odds ratio is >1 was performed. P-values for different neuron subtypes but the same function term were adjusted by the false discovery rate (FDR). For the enrichment analysis, we adjusted the functional annotation per neuron by sampling from $\{f|D(f, N_i) \leq D(f^*(N_i), N_i) + \alpha\}$, instead of using $f^*(N_i)$ directly. Here, $\alpha = 0.05$ is a small number adjusting the extent of relaxation. This adjustment helps to handle the cases with multiple minimums.

Determination of cortical laminar depth

As thickness of each laminar layer can vary across cortex, and the imaging result does not provide enough information to precisely delineate each layer, we did not attempt to systematically distinguish laminar layers in this study. Instead, we used a number in the range $[0, 1]$ to represent laminar depth, in which 0 denotes a position at the superficial cortical surface and 1 denotes a position at the boundary between white and grey matter.

Firstly, we extracted voxels in the reference atlas that have laminar depths 0 or 1, namely those boundary voxels of the cortical gray matter annotation. With S_0 and S_1 respectively denoting the two sets of voxels with depth 0 and 1, the depth at any cortical location P can be determined by:

$$\text{mindist}(P, S) \triangleq \min_{v \in S} |P - v|$$

$$\text{depth}(P) = \frac{\text{mindist}(P, S_0)}{\text{mindist}(P, S_0) + \text{mindist}(P, S_1)}.$$

We utilized K-Dimensional Tree (KD-Tree) to accelerate the minimum distance calculation. For a few samples, to eliminate laminar depth inaccuracies introduced by imperfect registration, we applied a similar computation in the sample space. In these cases, boundary voxels determined by manual image segmentation were used to define S_0 and S_1.

Comparison with population tracing

For the comparison to bulk tracing data from serial two-photon microscopy,[9] we calculated total neurite lengths contributed by neurons from injection site G97-1bL for each brain area. Then, the total length per brain area was compared against the "GFP volume" per brain area with linear regression analysis.

The fMRI data for comparison[10] provides vertex-level activity strength for the whole ipsilateral cortex. For comparison, we similarly calculated total neurite lengths of pooled single-neuron projectomes for each vertex, and compared total neurite length per vertex to cortical activity per vertex. Correlation analysis allowed us to identify the consistency between pooled single-neuron projectomes and fMRI activity data at electrical stimulation sites near our injection sites.

For the comparison to the connectome obtained by Markov et al.,[7] we firstly mapped brain areas of their connectome to the standard NMTv2 brain areas. The values of extrinsic fractions of labeled neurons (FLNe) from Markov et al.'s connectome were then compared to the average projection strengths of single neurons for each shared source brain area. Correlation tests of rank values were performed to assess the significance of the correlation between their connectome and our single-neuron projectome.

Segmentation of axon arbors

In this study, we segmented axon arbors based on axon morphology by machine learning, similar to our previous study on mouse axon arbors.[13] In our study, axon arbors were distinguished by a sudden decrease in branch length and a marked increase in branch density downstream of the axon tree, and/or the entrance to a cortical region (gray matter) or a subcortical nucleus. Such definition aligns with previous investigations of arbor morphology in both cortical and subcortical regions,[63–68] and we manually curated a training set of axon arbors of macaque neurons based on this definition. Then, the training set, after processing, was used to train a Graph Neural Network (GNN) that classifies graph vertices into two classes: arbor-positive vertices and arbor-negative vertices, as illustrated by the red and green branches of the dendrogram in Figure S3A, respectively. Finally, the trained GNN was applied to all neurons, and the GNN output, after processing, produced segmented axon arbors.

The GNN was applied to the dendrogram of axon terminals instead, not on the original axon tree. Using dendrograms has at least two advantages:

there are substantially fewer vertices in the dendrogram than in the original axon tree;
in the case when a collateral emerges from an axon arbor, a simple corresponding sub-tree representation for the axon arbor is usually possible in the dendrogram, but not possible in the original axon tree.

The dendrogram was produced by hierarchical clustering of axon terminals with Ward's linkage, using path distance between axon terminals.

We used the network in the ''GraphNeuralNetworks'' Julia package to implement axon arbor segmentation.

General arbor features

We used custom code to compute some of the general arbor features, including maximum (and 0.75 quantile) path distance to arbor root, number of branches, total length, maximum (and 0.75 quantile) distance between arbor nodes, convex hull volume, and length density with respect to volume.

Additionally, we used the L-Measure program[56] to compute extra arbor features. The following parameters displayed in Figure S8 were calculated as both average and sum:

branch path length (Branch_pathlength_avg/sum),
Euclidean distance (EucDistance_avg/sum),
terminal degree number (Terminal_degree_avg/sum),
helix (Helix_avg/sum).

The following parameters were calculated as average only:

local bifurcation amplitude (Bif_ampl_local_avg),
remote bifurcation amplitude (Bif_ampl_remote_avg),
local bifurcation tilt (Bif_tilt_local_avg),
remote bifurcation tilt (Bif_tilt_remote_avg),
local bifurcation torque (Bif_torque_local_avg),
remote bifurcation torque (Bif_torque_remote_avg),
branch order (Branch_Order_avg),
contraction (Contraction_avg),
fractal dimension (Fractal_Dim_avg),
fragmentation (Fragmentation_avg),
length (Length_avg),
partition asymmetry (Partition_asymmetry_avg),
path distance (PathDistance_avg).

The following parameters were calculated as sum only:

number of branches (N_branch_sum),
number of stems (N_stems_sum),
peak number (Pk_sum),
terminal segment number (TerminalSegment_sum).

Noted that we assume that convex hulls of arbors are spherical and define *arbor size* as the diameter of the convex hull:

$$D = \sqrt[3]{\frac{6}{\pi}\cdot \text{Volume}}.$$

For a non-spherical arbor, this formula is still used, providing a summary of the spans of the arbor along different axes.

Laminar distribution of arbors

For each arbor node, we calculated the depth value in the range $[0,1]$, using the method in the part "*Determination of cortical laminar depth*". A histogram with 101 bins ($[i/100-0.005, i/100+0.005]$ for $i = 0,1,\ldots,100$) weighted by segment length was then used to represent the laminar depth distribution of an axon arbor.

We pooled multiple arbors together to describe the laminar depth distribution of a certain group of axon arbors. The pooled histogram was smoothed and normalized.

To cluster arbors based on their laminar distribution, we calculated two distance measures between pairs of arbors:

2-norm of the difference between smoothed laminar depth histograms of the two arbors;
difference between the histogram entropies of the two arbors.

Hierarchical clustering was then performed with a distance matrix that combines these two distance measures by addition. We tuned the weight for addition to maximize mutual information between the arbors' distribution across the resulting arbor clusters and their spatial distribution in brain areas.

Detection of arbor patches

We detected arbor patches based on hierarchical clustering of axon arbors. The distance between arbors was calculated as

$$\mathrm{dist}(A,B) = \mathrm{median}_{a\in A}\left(\min_{b\in B}|a-b|\right),$$

where a and b denote nodes in arbors A and B, respectively. The resulting distance matrix $M = [\mathrm{dist}(A,B)]_{A,B}$ is asymmetric, but the symmetric matrix $(M+M')/2$ is used for hierarchical clustering.

The dendrogram after hierarchical clustering was cut to produce clusters of arbors, namely arbor patches. The height for tree cut was optimized to identify the arbor patches in the striatum. We applied this analysis separately for each sample, as cross-sample overlapping of single arbors is not meaningful due to sample variations and registration inaccuracy.

The average diameter of striatal arbor patches in Figure 5M was estimated by the distances between centers of adjacent arbor patches. We first performed single-linkage hierarchical clustering of arbor patch centers using Euclidean distance, which essentially connects all patch centers into a tree with minimum total edge length. In this tree, the 0.25 quantile of longest edges was discarded as they might connect centers of non-adjacent arbor patches. The lengths of the remaining edges were then used to estimate the average distance between adjacent striatal arbor patches. The sizes of the cortical arbor patches and arbor stripes, presented as examples in Figure S6E, were determined by manual measurements based on the results of single-neuron reconstructions.

Identification of intra-PFC subdomains

We defined cortical subdomains as areas containing dense reconstructed arbors/somata, allowing for fine-grained parcellation of standard macaque PFC areas in the reference atlas. The identification of subdomains was based on hierarchical clustering of cortical axon arbors and somata. The distance between two arbors, two somata or between one arbor and one soma was simply computed as the distance between their centers. Additionally, these centers were mapped onto a 2D cortical surface by setting their laminar depth value (as defined in the part "*Determination of cortical laminar depth*") as 0.5 in the calculation of their distances. Thus, two locations that only differed in their laminar depths were considered to be in the same subdomain.

Homo-/hetero-typic projection identification

Based on the cortical subdomains, we defined axon arbors in the mirrored subdomain of their somata as homotypic projections. The axon arbors distant from the mirrored somata subdomains, excluding the axon arbors in or neighboring the mirrored somata subdomains, were defined to be heterotypic.

Co-innervation analysis of PFC ITi neurons

For each specific soma-containing subdomain, we defined the binary projection matrix from neurons in this subdomain to all target subdomains based on the presence of corresponding axon arbors. Co-innervation was quantified by the pair-wise correlation matrix of the projection matrix, where a high value indicates that two subdomains are concurrently innervated by single neurons.

Calculation of F_1 scores along axon routes

We used F_1 scores to estimate the separation of two pre-defined types of neurons along the axon routes to a pre-defined target. With the pre-defined two types, we have two groups of neurons: positive (P) neurons and negative (N) neurons. At a cross-section along the routes, each neuron has a corresponding 2D coordinate (UV) in the cross-section plane. A line in the cross-section can be used to classify these neurons into two groups of predicted positive (PP) and predicted negative (PN) neurons. Thus, four cases can occur for each neuron: true positive ($TP = PP \cap P$), true negative ($TN = PN \cap N$), false positive ($FP = PP \cap N$), and false negative ($FN = PN \cap P$). The F_1 score for a line at a cross-section, i.e., a binary classification at the cross-section, is defined as:

$$F_1(PP,PN;P,N) = \frac{2|TP|}{2|TP|+|FP|+|FN|}.$$

The F_1 score is in the range $[0,1]$, and a value of 1 means correct prediction, implying that the two pre-defined types of neurons can be clearly separated at the cross-section by the line.

The F_1 score at a cross-section is the maximum of F_1 scores for all lines at the cross-section, i.e., $\max_{PP,PN} F_1(PP,PN;P,N)$, which is approximated by brute-force search in this study.

Topography index calculated along axon path

The topography index was calculated based on the F_1 score in the part "*Calculation of F_1 scores along axon routes*". But instead of two pre-defined types (P and N), many binary classifications of neurons at a cross-section ($\{(P,N)\}$) were enumerated. For each such binary classification, we searched a best F_1 score over all binary classification based on soma location ($\{(PP,PN)\}$):

$$F_1^*(P,N) = \max_{(PP,PN)} F_1(PP,PN;P,N).$$

The median value, and 0.25 and 0.75 quantiles of $\{F_1^*(P,N)\}$ were used as the measures of preservation of topography between soma locations and axon locations at a specific cross-section. If all three values are close to 1, topography is highly preserved along all directions. If only the 0.75 quantile is close to 1, topography is highly preserved only in a specific direction.

Definition of hemispheric bias index

To measure the bias of ITc/ITs neurons in sending arbors to the ipsilateral and contralateral hemispheres, we defined a simple *hemispheric bias index*

$$I_{\text{bias}}(N;A) = \frac{|N|_{A^c} - |N|_{A^i}}{|N|_{A^c} + |N|_{A^i}},$$

where $|N|_{A^i}$ and $|N|_{A^c}$ denote the total arbor lengths of neuron N in brain area A of the *ipsilateral* and *contralateral* hemispheres, respectively. The I_{bias} index takes on values in the range $[-1,1]$. A neuron of I_{bias} value -1 sends arbors only to the ipsilateral target area, while a neuron of I_{bias} value 1 sends arbors only to the contralateral target area. Neurons with equal projections to both hemispheres have I_{bias} values near 0.

Statistics

All linear regression analyses in this study employed a correlation test to calculate the Pearson correlation coefficient and the corresponding p-value to assess the statistical significance of the correlation. In Figure S1B, linear regressions and correlation tests were conducted to examine the relationship between the rank of GFP volume in bulk-tracing data and the rank of projection strength in our single-neuron projectome data, and linear regressions and correlation tests were also conducted to examine the relationship between the rank of fMRI activity in electric-stimulated fMRI data and the rank of projection strength in our single-neuron projectome data. In Figure S1D, linear regression and correlation test were conducted to examine the relationship between the rank of FLNe in bulk tracing data and rank of projection strength in our single-neuron projectome data in areas 8B, 9, 45b and 46d, respectively. In Figure 3H, linear regression and correlation test were conducted to examine the relationship between temporal arbor center and mediolateral soma position for neurons in subtypes 13 and 14. In Figure 3K, linear regression and correlation test were conducted to examine the relationship between arbor center and soma position on the mediolateral axis for neurons in subtypes 15 and 32. In Figure 4L, linear regression and correlation test were conducted to examine the relationship between dorsoventral arbor center and caudorostral soma position of ACgG-projecting dlPFC neurons. In Figure 5E, linear regression and correlation test were conducted to examine the relationship between the cross-section distribution of axons and soma position on the caudorostral axis for PFC ITc neurons. In Figure 5F, linear regression and correlation test were conducted to examine the trend of hemispheric bias index along the dorsoventral axis of soma position for PFC ITc neurons. In Figure S6A, linear regression and correlation test were conducted to examine the relationship between the cross-sectional distribution of axons and soma position on the dorsoventral axis for PFC ITc neurons. In Figure 6F, linear regression and correlation test were conducted to examine the relationship between mediolateral arbor center and mediolateral soma position of lPFC PT neurons. In Figure S7C, linear regression and correlation test were conducted to examine the relationship between mediolateral arbor center and mediolateral soma position within dlPFC PT neurons. In Figure 6J, linear regression and correlation test were conducted to examine the relationship between dorsoventral arbor center and mediolateral soma position of lPFC CT neurons. In Figure S7F, linear regression and correlation test were conducted to examine the relationship between the mediolateral arbor center in SC and the mediolateral soma position of mouse PFC PT neurons. In Figure S7G, linear regression and correlation test were conducted to examine the relationship between the dorsoventral arbor center in MD and the mediolateral soma position of mouse PFC CT neurons.

To determine whether there were statistically significant differences between groups, the two-sided Wilcoxon rank-sum test, a non-parametric method, was applied throughout this study. In Figure 3E, a two-sided Wilcoxon rank-sum test was conducted to compare the laminar depths of somata between subtypes 13 and 15. In Figure 3H, a two-sided Wilcoxon rank-sum test was conducted to compare the laminar depths of somata between subtypes 13 and 14. In Figure 4I, a two-sided Wilcoxon rank-sum test was conducted to compare the laminar depths of somata between ACgG- and OFC-projecting vlPFC neurons. In Figure 6P, two-sided Wilcoxon rank-sum tests were conducted to compare the differences between total arbor length, arbor size and number of arbor branches between lPFC PT and CT neurons. In Figure 7B, two-sided Wilcoxon rank-sum tests were conducted to respectively compare the differences of soma positions between neurons with temporal, LIP-, and RSC- projections in macaques and mice. In Figure 7K, two-sided Wilcoxon rank-sum tests were conducted to compare the differences in total axon length, number of branches, axon trunk length, number of collaterals, and normalized arbor size between macaques and mice within each subgroup of IT, CT, and PT. In Figure S8, two-sided Wilcoxon rank-sum tests were conducted to compare the differences in many morphological parameters calculated by L-measure[56] between macaques and mice within each subgroup of IT, CT, and PT.

To determine whether there were statistically significant differences between the laminar distribution of arbors involved in different projections, the two-sided Wilcoxon rank-sum test of mean laminar depth was applied throughout this study. In Figure 4F (right top), a two-sided Wilcoxon rank-sum test of mean laminar depth was conducted to compare the laminar depth distribution between arbors involved in dlPFC→vlPFC projection and somata of neurons with vlPFC→dlPFC projections. In Figure 4F (right bottom), a two-sided Wilcoxon rank-sum test of mean laminar depth was conducted to compare the laminar depth distribution between arbors involved in

vlPFC→dlPFC projection and somata of neurons with dlPFC→vlPFC projections. In Figure 4G (left), a two-sided Wilcoxon rank-sum test of mean laminar depth was conducted to compare the laminar depth distribution between arbors involved in area 45b→area 12r and area 12r→area 45b projections. In Figure 4G (right), a two-sided Wilcoxon rank-sum test of mean laminar depth was conducted to compare the laminar depth distribution between arbors involved in dlPFC→vlPFC and vlPFC→dlPFC projections. In Figure 4I, a two-sided Wilcoxon rank-sum test of mean laminar depth was conducted to compare the laminar depth distribution between arbors involved in vlPFC→ACgG and vlPFC→OFC projections. In Figure 5G, a two-sided Wilcoxon rank-sum test of mean laminar depth was conducted to compare the laminar depth distribution between arbors involved in the projection from dlPFC to contralateral regions, and the projection from vlPFC to contralateral regions. In Figure 6N, a two-sided Wilcoxon rank-sum test of mean laminar depth was conducted to compare the laminar depth distribution between CT arbors and PT arbors on the dorsoventral axis in MD. In Figure 7E, a two-sided Wilcoxon rank-sum test of mean laminar depth was conducted to compare the laminar depth distribution between PFC axonal arbors of macaques and mice in TE, RSC and LIP, respectively. In Figure S7E, a two-sided Wilcoxon rank-sum test of mean laminar depth was conducted to compare the laminar depth distribution between arbors involved in the projection from ORBvl/ORBl to contralateral regions in mice, and arbors involved in the projection from lPFC to contralateral regions in macaques.

For the combinations of homotypic and heterotypic projection patterns, proportion tests were conducted to evaluate whether the projections in various combinations were significantly enriched or depleted, with p-values adjusted using FDR correction. In Figure 5I, proportion tests followed by FDR correction were conducted to identify the significant increases or decreases of combinations of ipsilateral/contralateral ACgG projections and contralateral homotypic dlPFC projections. In Figure S6B, proportion tests followed by FDR correction were conducted to identify the significant increases or decreases of combinations of ipsilateral/contralateral striatal projections and contralateral lPFC projections.

In Figure 2D, Fisher's exact tests were conducted to calculate the significant association between each subtype and the biological functions. For each biological function, p-values were conducted FDR correction after Fisher's exact tests.

In Figure 7A, Fisher's exact test was conducted to calculate the significant association between soma location in ORBl/ORBvl and projections to RSP/PTLp.

For all significance marks of p-values used in this study, * $p < 0.05$; ** $p < 0.01$; *** $p < 0.001$.

Supplemental figures

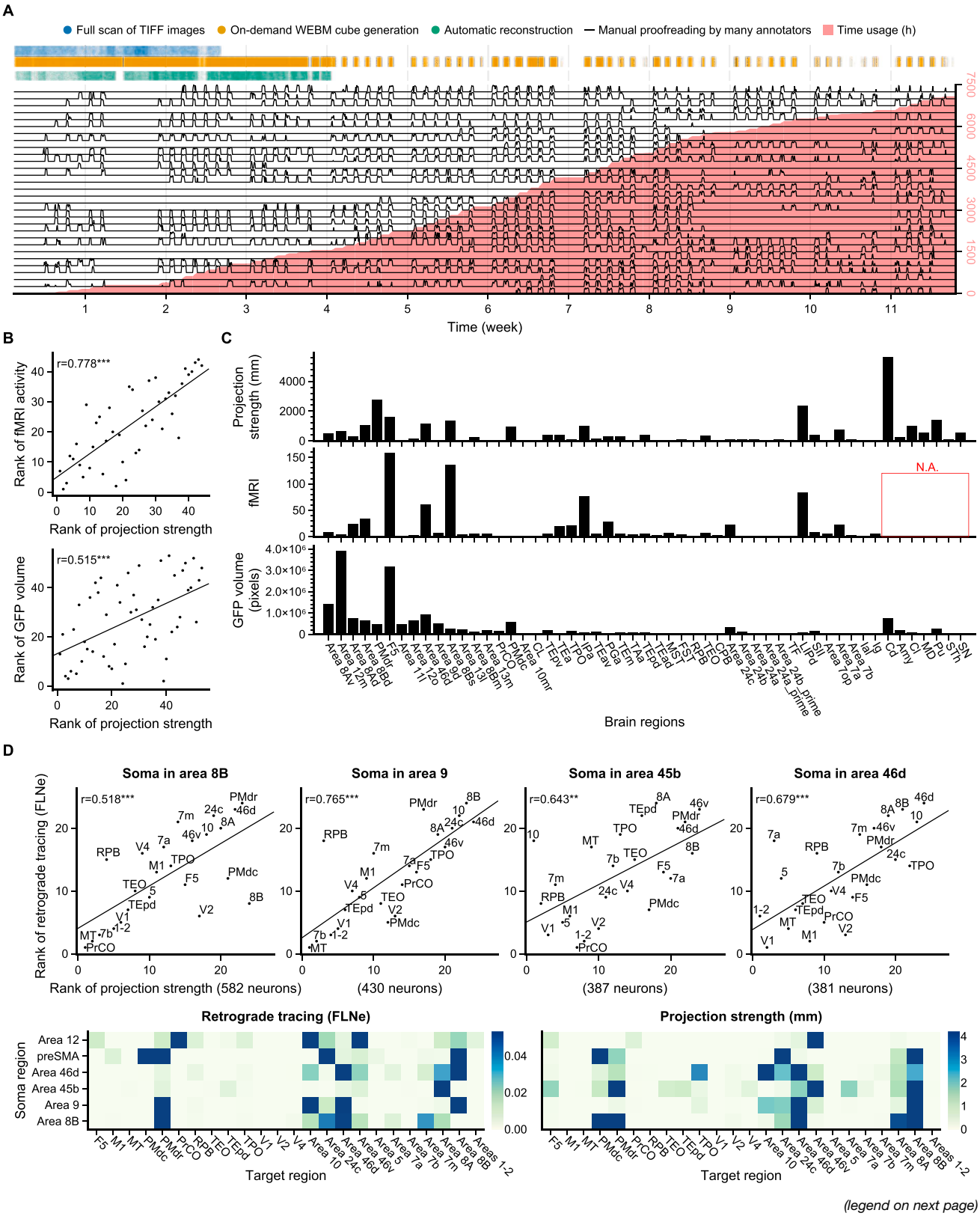

(legend on next page)

Figure S1. Progression timeline of single-neuron reconstruction for macaque dataset G97-1, and comparison of single-neuron projectomes with fMRI data upon electric stimulation, bulk tracing data using serial two-photon microscopy in area 45 of vlPFC, and whole-brain retrograde bulk tracing data, related to STAR Methods and Figure 1

(A) Summarized workflow of single-neuron reconstruction by Gapr[16] for the dataset G97-1 over 11 weeks is presented here, detailing the contributions of automated reconstruction and manual proofreading processes. The blue bars represent the initial full scan of Tagged Image File Format (TIFF) images, the orange bar shows on-demand data conversion of image cubes in Web Media (WEBM) data format, and the green bar indicates automatic reconstruction. Black lines mark manual proofreading by the randomly selected 30 annotators (from over 50 participants in total), while the light red shading represents the cumulative time usage in hours for all participants. The timeline highlights the interplay between automated processes and human intervention, with increasing manual efforts as the reconstruction progresses.

(B) Top: the scatterplot depicts the relationship between projection strengths of pooled single-neuron projectome data in ranks and fMRI activity strengths in ranks in area 45 of the vlPFC upon electrical stimulation in a previous publication.[10] Each dot represents a data point corresponding to a ranked measurement from these datasets. A significant positive correlation is observed, with a Pearson correlation coefficient of $r = 0.778$ (*** $p < 0.001$). The fitted regression line shows the positive linear relationship between pooled single-neuron projectomes and fMRI activity. Bottom: the scatterplot depicts the relationship between projection strengths of pooled single-neuron projectome data in ranks and the population-level projection strengths in ranks in area 45 of the vlPFC in a previous publication.[9] Each dot represents a data point corresponding to a ranked measurement from these datasets. A significant positive correlation is observed, with a Pearson correlation coefficient of $r = 0.515$ (*** $p < 0.001$). The fitted regression line shows the positive linear relationship between the ranks of pooled single-neuron projectomes and population-level projections.

(C) Barplots showing the projection strengths of pooled single-neuron projectome data (top), fMRI signals activated upon electric stimulation (middle), and the population-level projection strengths (bottom) across a set of brain areas. Note that only the data in ipsilateral cortical areas was provided in the original paper.[10] Thus, the subcortical areas were denoted as N.A. in fMRI data.

(D) Comparison between area-level projection strengths pooled from PFC neurons in single-neuron projectome data and the connectivity matrix reported by Markov et al.[7] Top: for neurons originating from four prefrontal soma regions (areas 8B, 9, 45b, and 46d), the extrinsic fractions of labeled neurons (FLNe) from bulk tracing data were compared with the projection strengths pooled from our single-neuron projectomes. The FLNe values reflect the relative projection strength to each target area as reported by Markov et al.[7] Pearson correlation coefficients (r) are shown. ** $p < 0.01$, *** $p < 0.001$. Bottom: projection strengths from six frontal regions (areas 12, preSMA, 46d, 45b, 9, and 8B) to downstream target areas. Left and right panels show the results from bulk tracing and single-neuron projectome data, respectively.

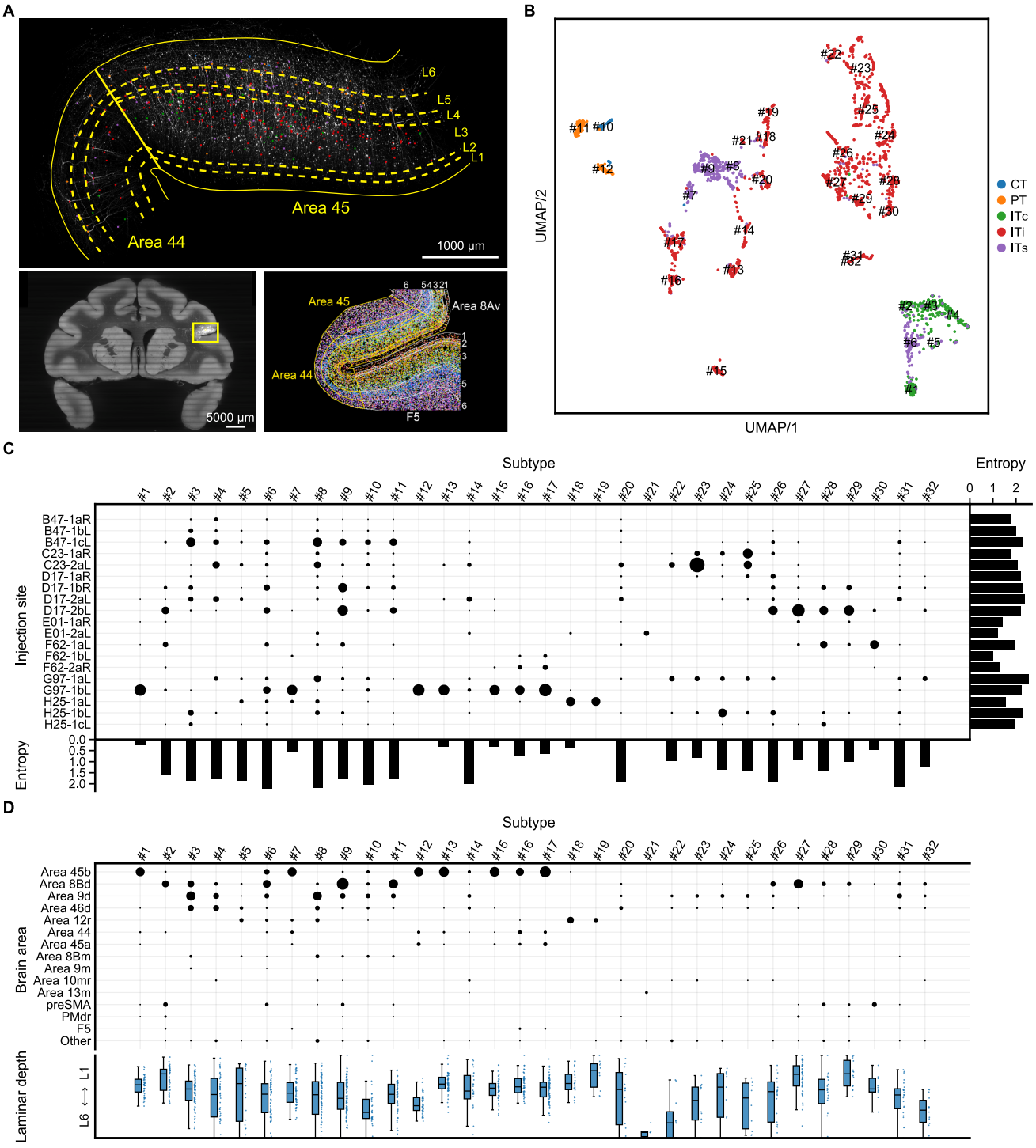

Figure S2. Demonstration of laminar soma distribution in the injection site G97-1bL and projectome-based classification of macaque PFC single-neuron projectomes, related to Figures 1 and 2

(A) Laminar distributions of somata of ITi, ITc, ITs, PT, and CT neurons in the injection site G97-1bL at area 45 in vlPFC (top; scale bar, 1,000 μm). The somata of each neuron type are color-coded according to Figures 1H–1I. A down-sampled original image of the coronal section is shown for the injection site containing the labeled neurons (bottom left; scale bar, 5,000 μm), and previously reported spatial transcriptome data[69] near the injection site are used as the reference for the definition of cortical layers in this area (bottom right).

(B) UMAP representation for the dissimilarities of axon morphology for all reconstructed neurons. The major neuron projection types are color-coded according to Figures 1H–1I. The identifiers (IDs) (#1–#32) of projectome-defined subtypes in Figure 2A are labeled on the UMAP.

(legend continued on next page)

(C) Distribution of projectome-defined subtypes in Figure 2A across injection sites. The size (area) of each black dot denotes the neuron number. Entropy measure for subtype complexity within each injection site and entropy measure for the complexity of injection site within each subtype are shown on the right side and bottom of the panel, respectively.

(D) Regional and laminar distributions of somata for projectome-defined subtypes in Figure 2A. The size (area) of each black dot denotes the neuron number. The boxplot of cortical soma depth for each subtype is bounded between 0 and 1, with the interquartile range (IQR) represented by the box, the whiskers lying within both the data range and 1.5 $\times$ IQR and the individual soma positions shown with dots on the right.

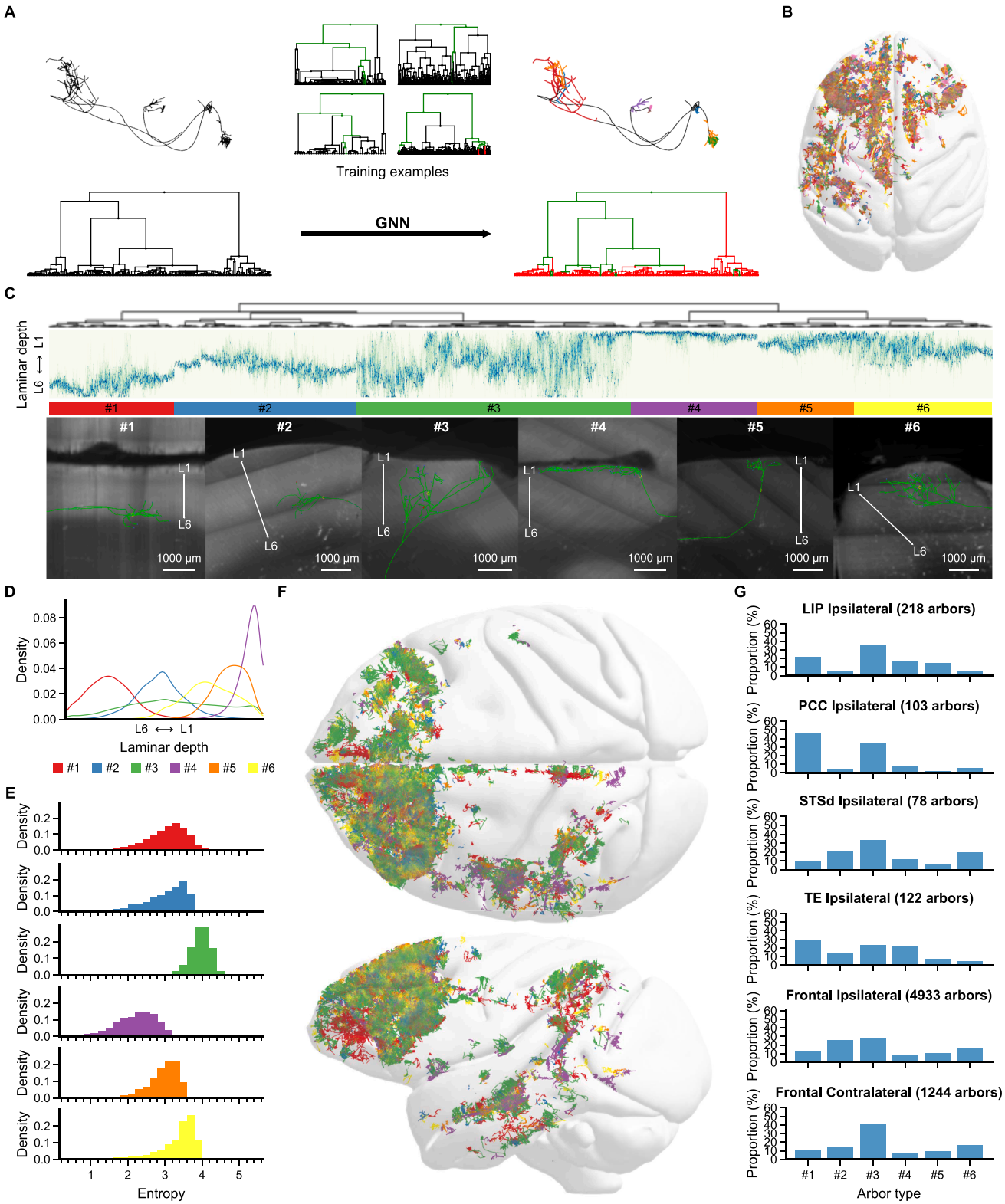

Figure S3. Segmentation of axon arbors by a machine learning algorithm, related to Figure 3

Machine learning models using graph neural networks (GNNs) were applied to accurately segment axon arbors based on subtree morphological features, followed by the analysis of arbor distribution across cortical layers.

(legend continued on next page)

(A) Schematic representation of axon arbor segmentation using GNN. Morphology of an axon before and after segmentation is shown in the upper left and upper right as an example, with their hierarchical structural organization represented by dendrograms below. The GNN classifies dendrogram vertices into arbor associated (red) and others (green), trained by manually currated training sets (upper center).
(B) 3D representation of segmented cortical and subcortical axon arbors in dataset G97-1. Each segmented axon arbor is randomly color-coded.
(C) Hierarchical clustering analysis reveals the laminar organization of cortical axon arbors, showing the differences of axon arbor distribution across cortical layers. Examples of reconstructed arbors belonging to the six subtypes are shown with actual fMOST images. The positions of the most superficial layer (L1) and the deepest layer (L6) of the cortex are labeled. Scale bars, 1,000 μm.
(D) Laminar distributions of axon terminal arbors for the six clustered subtypes.
(E) Entropy distribution reflecting the specificity of laminar distribution of each arbor type. Higher entropy values indicate broader layer distribution (corresponding to columnar pattern and diffusely expanded in multiple layers of arbor distribution), and lower entropy values indicated higher layer specificity (corresponding to specific layer distribution of arbors).
(F) A whole-brain example of six arbor types from dlPFC and vlPFC neurons in the representative datasets D17-1, D17-2, and G97-1.
(G) Proportions of arbor type distributions in the ipsilateral long-range cortico-cortical projection targets (LIP, PCC, STSd, and TE) and ipsi- and contralateral frontal target regions.

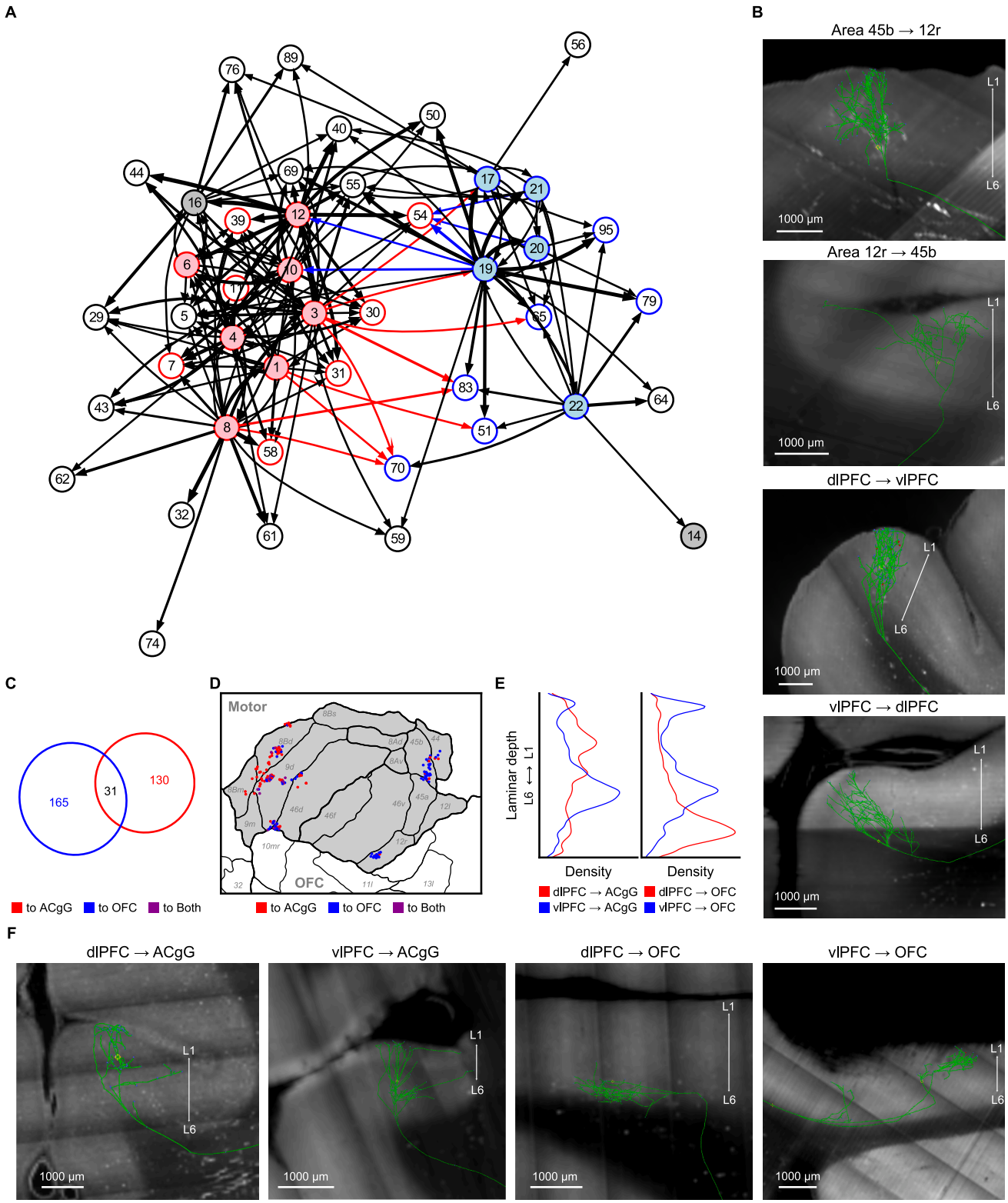

Figure S4. Subdomain network analysis of intra-PFC axon connections, related to Figure 4

(A) A graph representation of the intra-PFC network connectivity. Each node represents a subdomain within the PFC, and the edges indicate directed axonal projections between these subdomains. Numbers in the nodes are subdomain identifiers. Nodes in dlPFC and vlPFC are colored in red and blue, respectively. The

(legend continued on next page)

nodes with filled colors represent the subdomains containing at least 10 somata. The edges in the network representing dlPFC to vlPFC projections are colored in red, while those representing vlPFC to dlPFC projections are colored in blue. The widths of the edges represent the strengths of the projections.

(B) The laminar distribution of arborization in reciprocal projections between area 45b and area 12r (top two panels) and the laminar distributions of arborization in recurrent connections between the dlPFC and vlPFC (bottom two panels). The positions of the most superficial layer (L1) and the deepest layer (L6) of the cortex are labeled. Scale bars, 1,000 μm.

(C) Venn diagram showing the overlap of single axonal projections to ACgG (red) and OFC (blue). A total of 165 neurons project to ACgG but not OFC, 130 neurons project to OFC but not ACgG, and 31 neurons project to both ACgG and OFC.

(D) Soma distribution of neurons with projections to ACgG and OFC on the 2D flat map. Red dots indicate the somata of neurons projecting to ACgG but not OFC, blue dots indicate the somata of neurons projecting to OFC but not ACgG, and purple dots indicate the somata of neurons projecting to both ACgG and OFC.

(E and F) Laminar distribution of axon arbors of neurons in lPFC with projections to ACgG (E, left) and OFC (E, right). Density plots represent the laminar distribution of axon arbors of neurons in dlPFC (red) and vlPFC (blue) across cortical layers (L1-L6). Examples are shown in (F). The positions of the most superficial layer (L1) and the deepest layer (L6) of the cortex are labeled in (F). Scale bars in (F), 1,000 μm.

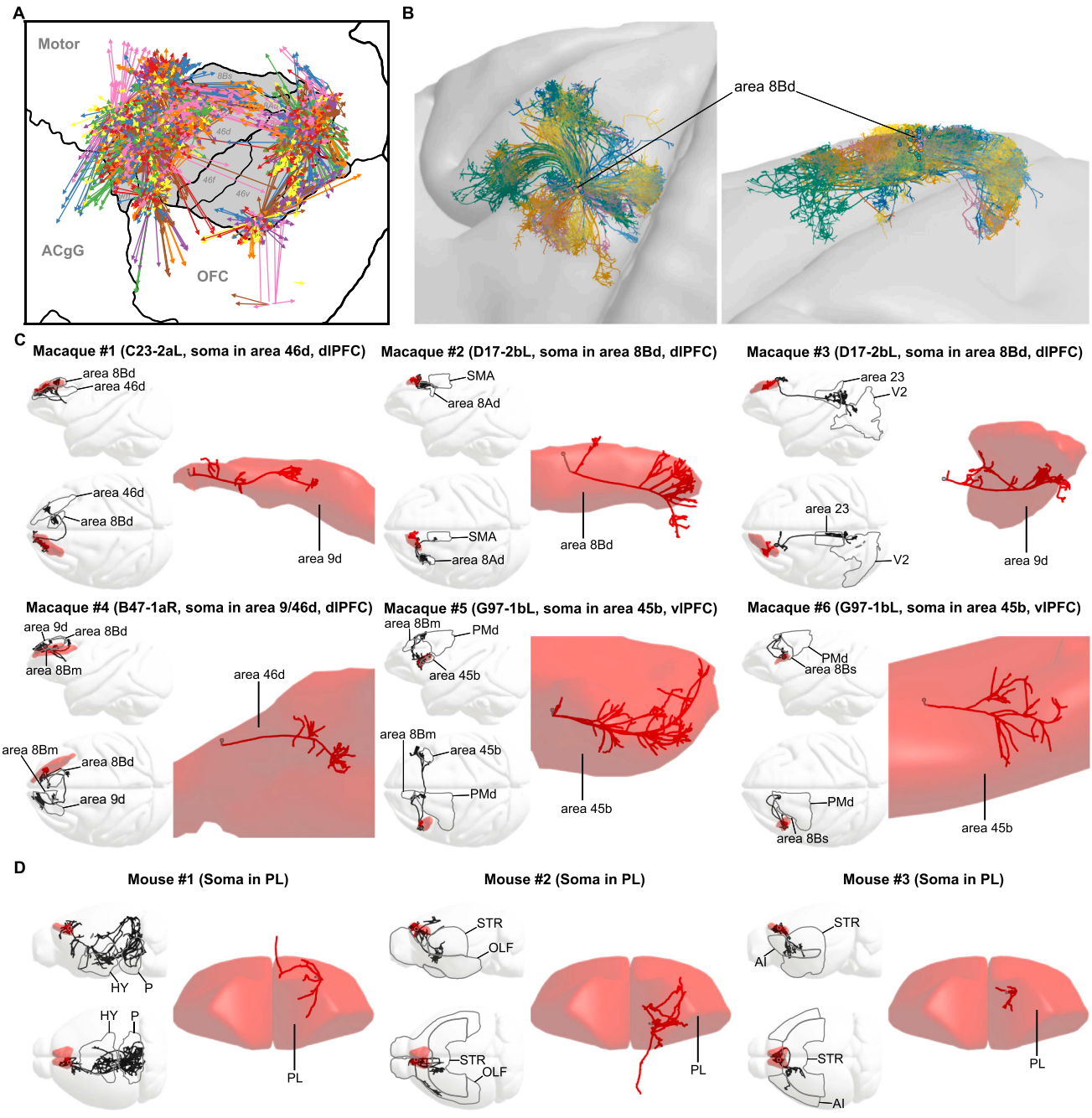

Figure S5. Intrinsic axon connectivity in PFC, related to Figure 4

(A) Intrinsic axonal projections within the PFC. Arrows originating from distinct regions represent the areas with concentrated distributions of neuronal somata. The arrows of various colors extending from each soma region denote the clustering types of intrinsic axons formed by neurons in that region. An arbor is considered an intrinsic arbor if its maximum cortical depth does not surpass 0.9 (scaled between 0 and 1 as the safety threshold for intrinsic axons), meaning that the arbor will definitively remain within the cortex and never extend into the white matter.

(B) Single intrinsic axons extensively arborized within area 8Bd and the adjacent cortical regions. Left and right panels show horizontal and coronal views, respectively. Intrinsic axons and their corresponding somata (dots) are randomly color-coded.

(C) Representative intrinsic axons in the PFC of macaques. Four examples from macaque dlPFC are shown—the first (Macaque #1) with soma in area 46d and intrinsic axon in area 9d, the second (Macaque #2) with both soma and intrinsic axon in area 8Bd, the third (Macaque #3) with soma in area 8Bd and intrinsic axon in area 9d, and the fourth (Macaque #4) with soma in area 9/46d and intrinsic axon in area 46d. Two examples from macaque vlPFC (Macaque #5 and Macaque #6), both with soma and intrinsic axon located in area 45b. Sagittal and horizontal views are shown on the left. The injection sites of these neurons are also mentioned in the title. Red mesh highlights the target region of the intrinsic axon in both views. The gray outlines in the left views mark the principal projection areas of the neuron. Intrinsic axonal fibers are shown in red, while all other axonal fibers are displayed in black.

(legend continued on next page)

(D) Examples of single intrinsic axons in mouse PFC, with soma and intrinsic axons both located in the dorsal part of the prelimbic area (PL). Mouse neurons in this study were registered to the Allen Mouse Common Coordinate Framework (CCF).[55] Sagittal and horizontal views are shown on the left. Red mesh highlights the target region of the intrinsic axon in both views. The gray outlines in the left views mark the principal projection areas of the neuron. Intrinsic axonal fibers are shown in red, while all other axonal fibers are displayed in black.

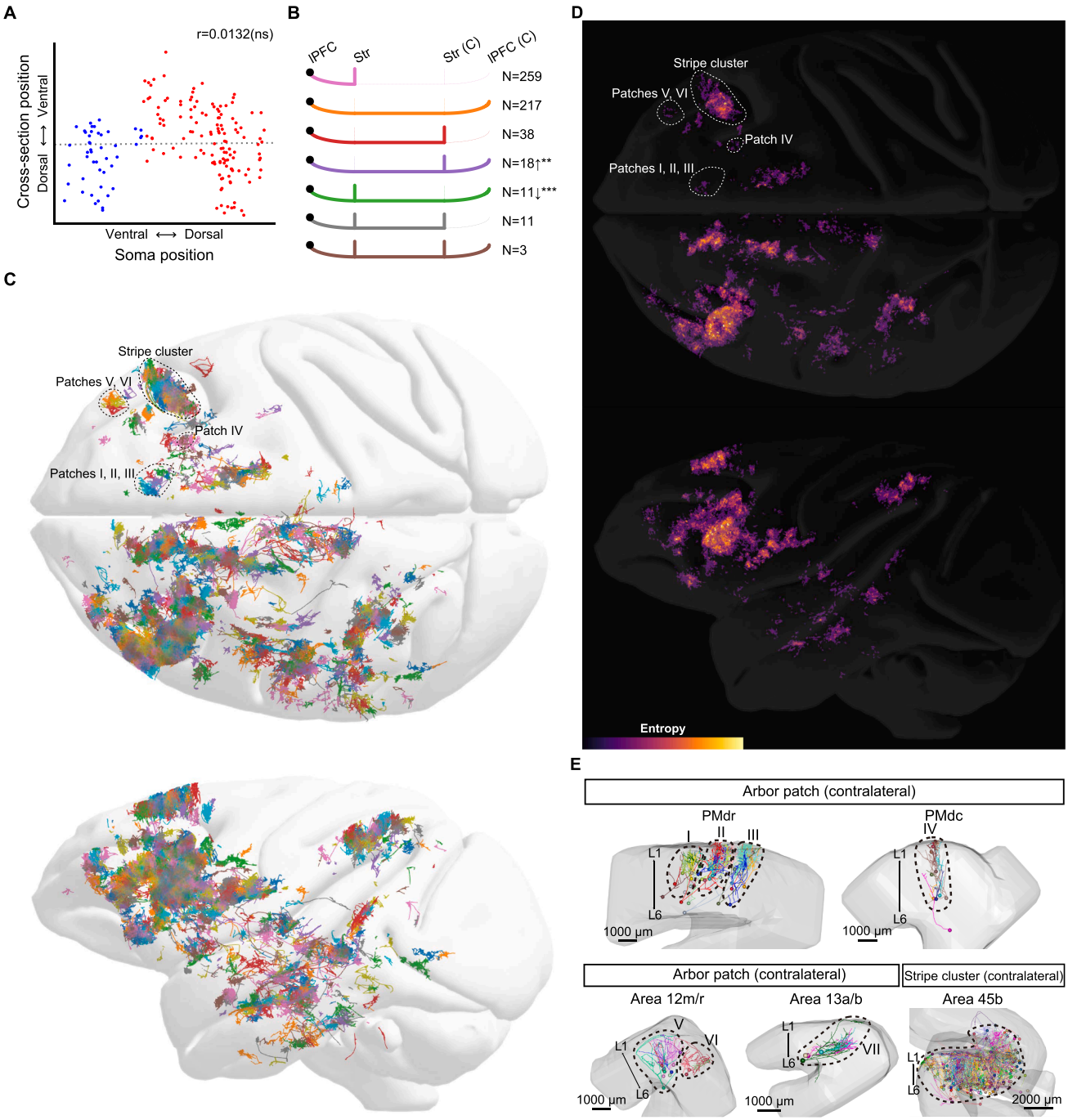

Figure S6. Contralateral and striatal projections of macaque PFC ITc/ITs neurons and systematic identification of arbor patches and stripes in the macaque brain (dataset G97-1), related to Figure 5

(A) The axon topography along the dorsoventral axis of ITc neurons in the PFC. Scatterplot showing the relationship between the soma position (*x* axis, ventral to dorsal) and the midline cross-sectional axon position of PFC ITc neurons (*y* axis, dorsal to ventral) along the dorsoventral axis. Each dot represents an individual axon, with blue and red dots corresponding to vlPFC and dlPFC axons, respectively. The correlation analysis (r = 0.0132; ns, not significant) shows that the topography of the soma location along the dorsoventral axis is not significantly correlated with the axon location at the midline cross-section of the corpus callosum, indicating that the soma position is not preserved in its axon location in this axis.

(B) The target preferences of ITs/ITc neurons in the PFC. Schematic representation showing the bilateral projection patterns of ITs/ITc neurons from the lateral PFC (lPFC) to homotypic cortical area and heterotypic target in the contralateral hemisphere when considering striatum as a heterotypic target (see Text). The seven combinations of projection patterns to ipsilateral striatum, contralateral lPFC, and contralateral striatum are shown, labeled as bold lines for each combination pattern. The numbers of neurons associated with each projection pattern are displayed on the right. Significantly enriched (the upward arrow) or

(legend continued on next page)

under-represented (the downward arrow) projection patterns, determined by proportion tests, are annotated with p values (** $p < 0.01$, *** $p < 0.001$). Note that ITc neurons that project to both the contralateral lPFC and contralateral striatum are significantly enriched.

(C) Visualization of IT axon arbor patches identified across cortical regions of the injection site G97-1bL. Arbors in each arbor patch are randomly color-coded. Each identified arbor patch area is labeled with a Roman numeral, and the arbor stripe area is labeled directly by text.

(D) The distribution of entropy measure to quantify the convergent projections from multiple neurons into the same patch (top: horizontal view; bottom: sagittal view) for the arbors in (C). High entropy value represents patches receiving multi-neuronal projections. Each identified arbor patch area is labeled with a Roman numeral as (C), and the identified arbor stripe area is labeled with the same region as (C).

(E) Detailed views of example arbor patches and stripes in the contralateral regions from dataset G97-1. Arbors in each arbor patch/stripe are randomly color-coded. Top and bottom left: individual arbor patches are in dashed outlines. Each identified arbor patch area is labeled with the same Roman numeral as (C) and (D). The patch VII is not shown in (C) and (D) because it comes from neurons in another injection site, G97-1aL. Scale bars, 1,000 μm. Bottom right: examples of arbor stripes observed in the contralateral area 45. The identified arbor stripe area is labeled with the same region as (C) and (D). Scale bar, 2,000 μm.

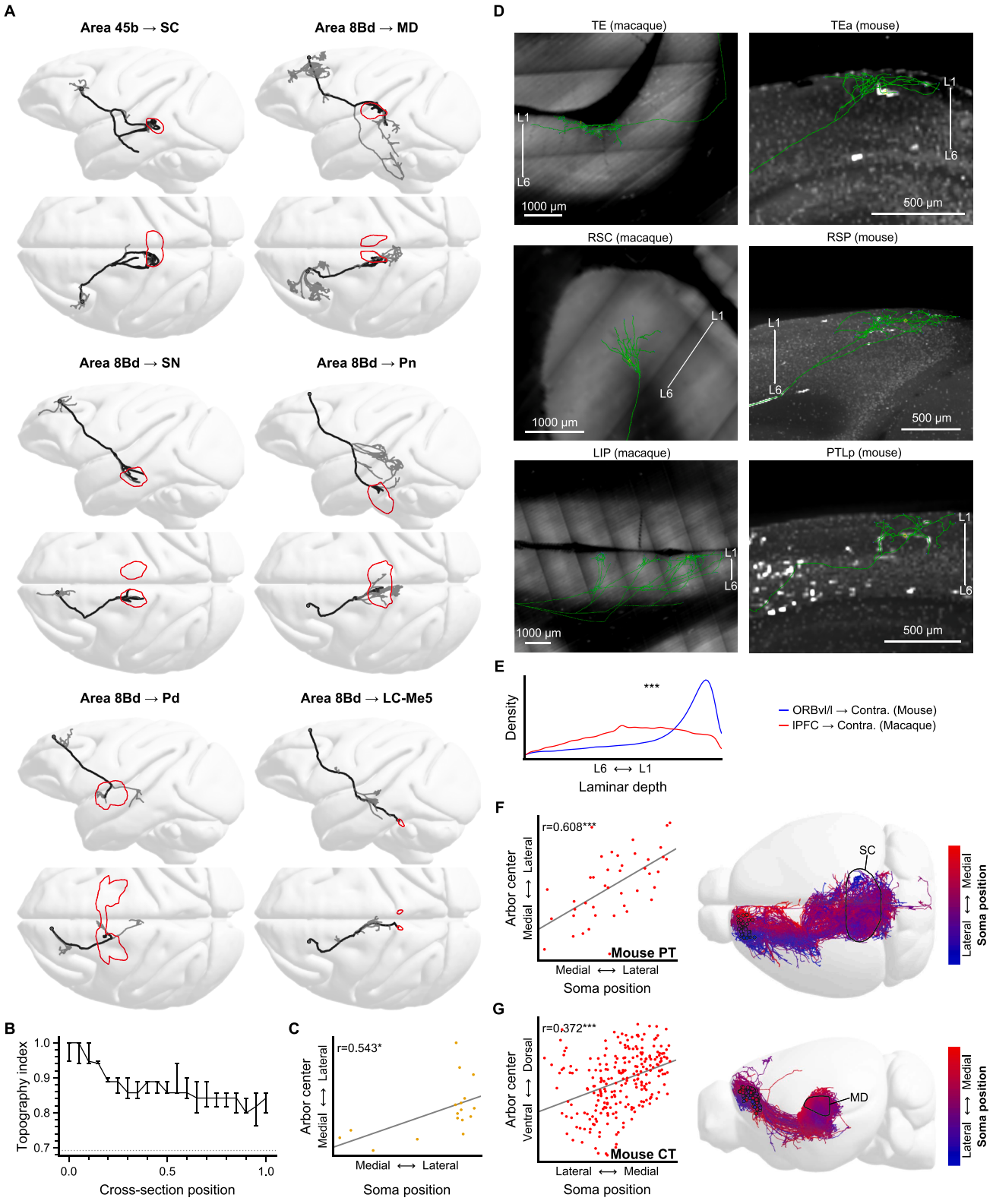

(legend on next page)

Figure S7. Topography and terminal arborization of macaque dlPFC PT neuron axons, their projections to typical targets, and comparative analysis of macaque and mouse PFC single-neuron projectomes, related to Figures 6 and 7

(A) Sagittal and horizontal views illustrating the projection patterns of individual PT neurons to representative target regions in the macaque brain. The soma location and the corresponding target area of each neuron are shown at the top. For each neuron, the main axonal trunk leading to each target, as well as its arborizations within the target area, are shown in bold black. Target regions are colored in red. Other parts of the axon are colored in gray.

(B) Topography indices are plotted against the normalized cross-section position of subcortical projections originating from macaque dlPFC PT neurons. The topography index measures the preservation of spatial organization across the cross-section, and the line and bars of topography index indicate the 0.25, 0.5, and 0.75 quantiles. The topography index declines steadily from the medial to lateral positions of the cross-section, indicating a decrease in topographic organization as projections extend laterally.

(C) The scatterplot shows the relationship between soma position and arbor center position for macaque dlPFC PT neurons on the mediolateral axis. Each point represents a single neuron. Pearson's correlation coefficient r is shown. $*p < 0.05$.

(D) Representative examples of terminal arborization patterns of single PFC neurons in macaque TE, RSC, and LIP, and their similar areas in mouse: TEa, RSP, and PTLp. Similar laminar distributions of terminal arbors are observed between TE (macaque) and TEa (mouse), as well as LIP (macaque) and PTLp (mouse). RSC (macaque) and RSP (mouse) arbors exhibit different laminar distributions. The positions of the most superficial layer (L1) and the deepest layer (L6) of the cortex are labeled. Scale bars, 1,000 μm for macaque and 500 μm for mouse neurons.

(E) Laminar distribution of terminal arbors in the contralateral cortex of mouse and macaque PFC ITc neurons. The blue line represents mouse ORBvl/ORBl neurons, and the red line represents macaque lPFC neurons. Mouse arbors are more concentrated in the superficial layers (closer to L1) compared with macaque arbors. $***p < 0.001$.

(F) Relationship between arbor centers in SC and soma locations of PT neurons in PFC along the mediolateral axis in the mouse brain. Mouse PT axons were colored according to their soma locations along the mediolateral axis (right). Pearson's correlation coefficient r is shown. $***p < 0.001$.

(G) Relationship between arbor centers in MD (along the dorsoventral axis) and soma locations of CT neurons in PFC (along the mediolateral axis) in the mouse brain. Mouse CT axons were colored according to their soma locations along the mediolateral axis (right). Pearson's correlation coefficient r is shown. $***p < 0.001$.

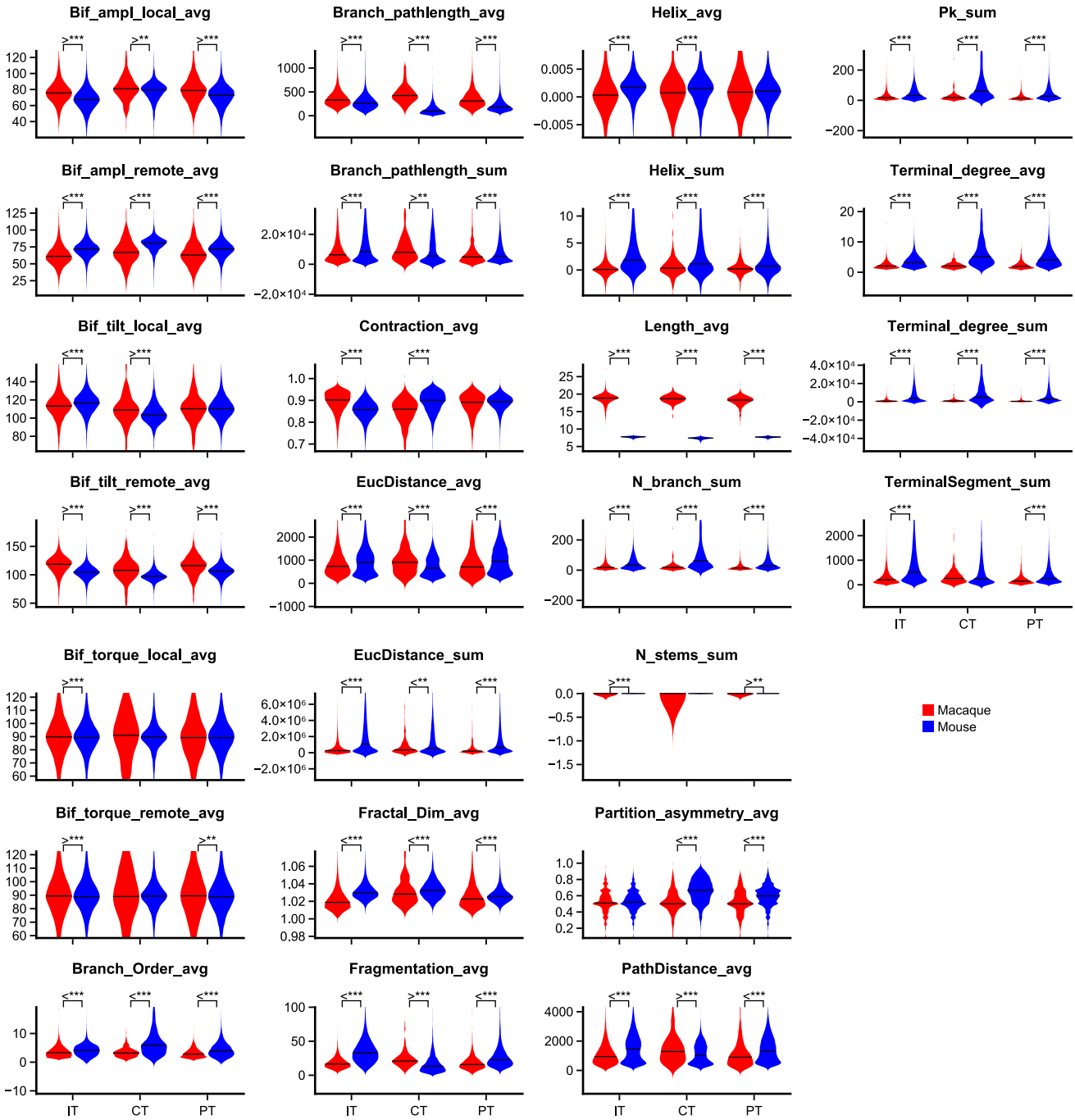

Figure S8. Comparison of general morphological features of PFC single-neuron projectomes between macaque and mouse, related to Figure 7

Violin plots comparing various general morphological features of IT, CT, and PT neurons between macaques (red) and mice (blue). These features are calculated by L-measure[56] and include average (avg) and sum measurements for different morphological features, such as bifurcation amplitude (Bif_ampl), bifurcation torque (Bif_torque), bifurcation tilt (Bif_tilt), fractal dimension (Fractal_Dim), branch order (Branch_Order), fragmentation, contraction, Euclidean distance (EucDistance), path distance, terminal degree, and length metrics. The median values are labeled with black lines. The greater-than (>) and less-than (<) signs represent the relative magnitude of the left and right data when significant differences are observed. Statistically significant differences between groups are denoted by ** $p < 0.01$ and *** $p < 0.001$.